

AD-A196 754

RADC-TR-88-52
Final Technical Report
April 1988

DTIC FILE COPY

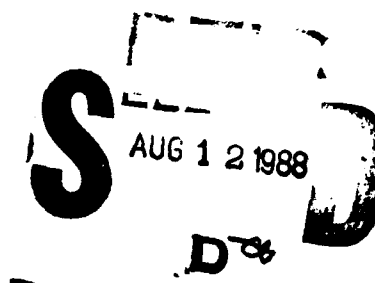


4

ELECTRON AND PHOTON TRANSPORT CALCULATIONS BETWEEN 1MeV AND 1eV

Arcon Corporation

Stanley Woolf



APPROVED FOR PUBLIC RELEASE; DISTRIBUTION UNLIMITED.

ROME AIR DEVELOPMENT CENTER
Air Force Systems Command
Griffiss Air Force Base, NY 13441-5700

UNCLASSIFIED

SECURITY CLASSIFICATION OF THIS PAGE

REPORT DOCUMENTATION PAGE				Form Approved OMB No. 0704-0188		
1a. REPORT SECURITY CLASSIFICATION UNCLASSIFIED			1b. RESTRICTIVE MARKINGS N/A			
2a. SECURITY CLASSIFICATION AUTHORITY N/A			3. DISTRIBUTION/AVAILABILITY OF REPORT Approved for public release; distribution unlimited.			
2b. DECLASSIFICATION/DOWNGRADING SCHEDULE N/A						
4. PERFORMING ORGANIZATION REPORT NUMBER(S) N/A			5. MONITORING ORGANIZATION REPORT NUMBER(S) RADC-TR-88-52			
6a. NAME OF PERFORMING ORGANIZATION ARCON Corporation		6b. OFFICE SYMBOL (If applicable)		7a. NAME OF MONITORING ORGANIZATION Rome Air Development Center (ESRE)		
6c. ADDRESS (City, State, and ZIP Code) 260 Bear Hill Road Waltham MA 02154			7b. ADDRESS (City, State, and ZIP Code) Hanscom AFB MA 01731-5000			
8a. NAME OF FUNDING/SPONSORING ORGANIZATION Rome Air Development Center		8b. OFFICE SYMBOL (If applicable) ESRE		9. PROCUREMENT INSTRUMENT IDENTIFICATION NUMBER F19628-83-C-0017		
8c. ADDRESS (City, State, and ZIP Code) Hanscom AFB MA 01731-5000			10. SOURCE OF FUNDING NUMBERS			
			PROGRAM ELEMENT NO. 61102F	PROJECT NO. 2306	TASK NO. J3	WORK UNIT ACCESSION NO. 33
11. TITLE (Include Security Classification) ELECTRON AND PHOTON TRANSPORT CALCULATIONS BETWEEN 1MeV AND 1eV						
12. PERSONAL AUTHOR(S) Stanley Woolf						
13a. TYPE OF REPORT Final		13b. TIME COVERED FROM Nov 82 TO May 86		14. DATE OF REPORT (Year, Month, Day) April 1988		
15. PAGE COUNT 80						
16. SUPPLEMENTARY NOTATION N/A						
17. COSATI CODES			18. SUBJECT TERMS (Continue on reverse if necessary and identify by block number)			
FIELD	GROUP	SUB-GROUP	electron transport; coupled electron-photon transport; photon transport; charge distributions in insulators, <i>gates</i>			
03						
19. ABSTRACT (Continue on reverse if necessary and identify by block number)						
<p>In this report we will describe the development and application of numerical methods for predicting dose and dose variation in multi-layered structures due to x-rays and gamma rays and the charge build-up in dielectrics due to electron beam irradiation. The scope of our work included: development and implementation of: 1) discrete ordinates electron transport calculations for electron sources both within and incident of solid structures; 2) discrete ordinates electron transport calculations for photon sources incident on layered solids; 3) Monte Carlo calculations and statistical analysis programs for low-energy electron transport in insulating structures. In addition, several photon transport calculations were made to determine the scattered photon energy spectra characteristic of various standard irradiation test facilities. <i>Woolf, S.</i></p>						
20. DISTRIBUTION/AVAILABILITY OF ABSTRACT <input checked="" type="checkbox"/> UNCLASSIFIED/UNLIMITED <input type="checkbox"/> SAME AS RPT <input type="checkbox"/> DTIC USERS			21. ABSTRACT SECURITY CLASSIFICATION UNCLASSIFIED			
22a. NAME OF RESPONSIBLE INDIVIDUAL JOHN C. GARTH			22b. TELEPHONE (Include Area Code) (617) 377-2360		22c. OFFICE SYMBOL RADC (ESRE)	

DD Form 1473, JUN 86

Previous editions are obsolete.

SECURITY CLASSIFICATION OF THIS PAGE

UNCLASSIFIED

TABLE OF CONTENTS

<u>Section:</u>	<u>Page</u>
I. INTRODUCTION	1
II. DISCRETE ORDINATES CALCULATIONS OF DOSE PROFILES IN MULTI-LAYERED STRUCTURES	3
1. Introduction	3
2. Discrete Ordinates Electron Transport Calculations for Monodirectional Electron Sources	4
3. Determination of Electron and Gamma-Ray Induced Dose Enhancement and Atomic Displacement Damage in Gallium Arsenide and Silicon	21
4. Calculation of the Electron Flux Energy Spectrum Near a Two Medium Interface	27
5. Determination of Scattered Cobalt-60 Photon Spectrum with ONETRAN Photon Dose Profile Calculations	30
6. Input Processor Programs for ONETRAN Electron Transport Calculations	37
III. MONTE CARLO CODE (MCSS) FOR THE ANALYSIS OF ELECTRON TRANSPORT IN INSULATING STRUCTURES AND ASSOCIATED STATISTICAL ANALYSIS COMPUTER CODES	40
1. Introduction	40
2. Electron Transport Model	40
3. Program Description	41
4. Statistical Analysis Computer Codes for the Analysis of Charge Distributions in Insulators as Calculated by the MCSS Monte Carlo Code	48
IV. PHOTON TRANSPORT CALCULATIONS WITH THE MCNP COMPUTER CODE	56
1. MCNP - General Description	56
2. Concrete-Walled Room Irradiation Chamber	56

3. AECL Gammacell 220	60
4. NBS Water Well Irradiator	63
5. MCNP Calculations for the Estimation of Filtration of Low Energy Components of Scattered Photon Spectra by Lead Cylinder Shields	63
V. REFERENCES	69

DATE: 12/1/77 TIME: 10:00 AM BY: [Signature] FOR: [Signature]	
BY: [Signature] DATE: 12/1/77	
FOR: [Signature]	
DIST: A-1	FOR: [Signature] DATE: 12/1/77



I. INTRODUCTION

During the period from November 4, 1982 through May 4, 1986, our work was directed toward the development and implementation of efficient numerical methods for predicting doses in multi-layered structures, such as metallized semiconductors, due to the incidence of x- and gamma radiation, and the calculation of charge distribution build-up in dielectrics due to electron beam irradiation. In the performance of this contract, electron transport calculations were made employing two fundamentally different methods, the method of discrete ordinates, which is a deterministic numerical method for obtaining approximate solutions of the electron transport equation, and Monte Carlo, a stochastic method for the simulation of particle trajectories and scattering interactions. The results of these calculations were reported in the seven technical papers published and four presentations given by the principal investigator during the course of this contract. Photon transport calculations were also made, using the Monte Carlo method, to provide information on Co-60 scattered photon spectra for dosimetry studies.

The discrete ordinates electron transport calculations were made using the ONETRAN¹ computer code. With our modified version of this code we calculated: (1) energy deposition in aluminum and gold due to the presence of 200 keV electron beam sources located on the vacuum boundary of a semi-infinite medium and embedded within an infinite medium; (2) dose enhancement, due to the incidence of Co-60 gamma radiation, in layered media, such as Au/Si (this notation is adopted throughout this document to denote, in this case, a 2-layer medium, i.e. gold-silicon); (3) atomic displacement damage in Si and GaAs due to exposure to 1.25 MeV gamma radiation and 600 and 1200 keV electron beams; (4) dose profiles in two- and three-layered media, Au/Al, Al/Au/Al, C/Al/Au, for ten monoenergetic photon sources, ranging in energy from 200 keV to 1250 KeV, and two photon directions, for the purpose of determining the Co-60 photon source spectrum which resulted in a set of experimental dose-profile data; and (5) electron flux energy spectra at and near Al/Al, Au/Al, and Au/Au interfaces due to isotropic, uniformly distributed (half-space) electron sources ranging in energy from 50 keV to 500 keV. The above discrete ordinates electron transport calculations are discussed in Chapter II.

Monte Carlo electron transport calculations were performed using two computer codes: (1) a low energy single scattering Monte Carlo program which we have developed to calculate and store electron tracks for energies ranging from 600 keV down to a few eV in thin silicon dioxide films; and (2) the TIGER² code, which calculates energy and charge deposition profiles, as well as emergent electron energy spectra, for primary and secondary electron sources. The low energy single scattering Monte Carlo

program and related statistical analysis programs are discussed in Chapter III. The TIGER² calculations were made in conjunction with the ONETRAN¹ discrete ordinates electron transport work, primarily for the purpose of providing independent benchmark calculations of energy deposition profiles. Some of these Monte Carlo results are reported in Chapter II, generally as histogram data for comparison with the discrete ordinates calculations.

Finally, Chapter IV is a report on a set of photon Monte Carlo calculations made for various Cobalt-60 irradiation sources. The purpose of these calculations was to provide a basis for comparison of photon spectrum hardness for various irradiation facilities both within and without the defense community. This spectrum information is directly applicable to the determination of dose enhancement in metallized semiconductor devices under test. The results of these Monte Carlo calculations have been incorporated in an ASTM³ standard on radiation hardness testing of electronic devices and materials.

II. DISCRETE ORDINATES CALCULATIONS OF DOSE PROFILES IN MULTI-LAYERED STRUCTURES

II.1 Introduction

Calculations of dose profiles in multilayered structures due to the presence of ionizing radiation sources such as electron beams, x-and gamma-radiation were made using a modified version of ONETRAN¹. Results of these calculations are reported in several publications⁴⁻⁶ in which the method of discrete ordinates is applied to electron transport problems where the source of radiation has been either an electron beam or a photon beam. Some of this work involved development of basic discrete ordinates algorithms, such as the method of streaming rays and comparisons with standard discrete ordinates methods⁴⁻⁶. In some instances evaluations were made of the accuracy of discrete ordinates methods for charged particle transport by comparisons with analytical benchmark calculations⁶ and other independent calculation methods such as the method of moments⁹. Recently, a paper was published in which the method of discrete ordinates was applied to obtain dose profiles, displacement damage rate profiles and electron flux spectra in GaAs and Si for both electron beams and gamma rays⁶. Many of these calculations were made for layered structures of GaAs or Si next to Au. This paper provides a very good demonstration of our ability to apply discrete ordinates methods to obtain solutions to practical problems in radiation effects in solids. Additionally, two recent papers resulting from our work involved, in one case, the application of the method of discrete ordinates to obtain electron flux energy spectra resulting from uniformly distributed, isotropic, half-space electron sources at and near two material interfaces. In the other instance, discrete ordinates calculations were made to determine the scattered Co-60 photon spectrum present in an experiment in which a set of dose profile measurements near material interfaces were made using a multi-layer ionization chamber technique. All of the above mentioned work will be described in further detail. This chapter will end with a brief description of the input data generation programs which we have written to facilitate the use of ONETRAN as an electron transport code.

II.2 Discrete Ordinates Electron Transport Calculations for Monodirectional Electron Sources

In the development of the method of discrete ordinates as a useful tool for obtaining electron energy and charge distributions, it is both necessary and desirable to compare the results obtained with this method with as many independent calculations as is practicable. In this way, the strengths and shortcomings of our calculation method can be identified and analyzed. One of the first set of such tests that we performed on the multigroup discrete ordinates method was a comparison of the results obtained with those of two other methods, another discrete ordinates method, the method of streaming rays, and with the Monte Carlo method. These tests were performed for an monodirectional electron source incident on semi-infinite aluminum slabs.⁴ In another set of calculations, the multigroup discrete ordinates method was compared again with the streaming ray method, the method of moments and an analytical benchmark calculation for a plane electron source embedded in an infinite scattering medium.⁶ As will be shown, the principal disadvantage associated with the multigroup discrete ordinates calculation method is found to be the problem of numerical straggling introduced by discretization of the electron energy. We have concluded, however, that the advantage afforded by the flexibility of the multigroup discrete ordinates method outweighs this disadvantage, at least in the energy range for which we have made our calculations (100 to 1250 keV). The ONETRAN code can be applied to any reasonable number of material layers and can be adapted to accommodate a wide variety of source configurations.

II.2.1. Electrons Incident on Aluminum⁴

Transport calculations were performed for 200 keV monodirectional electron sources incident on semi-infinite aluminum slabs. Two slab thicknesses were taken, 0.02 g/cm² and 0.04 g/cm². The calculations were performed using three different methods: 1) multigroup discrete ordinates (ONETRAN-S_N); 2) discrete ordinates based on the method of Streaming Rays; 3) the Monte Carlo method. The latter two methods were chosen for comparison with the multigroup method because each of these contains unique advantages in the process of testing multigroup discrete ordinates. The Streaming Ray method provides an alternative discrete ordinates approach to the electron transport problem. It is a numerical solution of the Spencer-Lewis⁴ form of the transport equation in which the electron flux is obtained as a function of position, angle and path length. The stopping power is used to relate the electron energy distribution to the path length distribution. The principal advantage of this method is that artificial straggling effects due to energy discretization are virtually eliminated. Thus, when results

obtained with the two discrete ordinates methods are compared, a direct observation of the effect of the straggling introduced by the multigroup approximation is possible, and methods for limiting this effect can be devised.

The third method, Monte Carlo, provides a completely independent means for computing the electron energy deposition and emergent electron energy spectra. Thus it serves as a check on both discrete ordinates methods, a benchmark. The Monte Carlo program chosen for this task is the well-known TIGER² code.

While much of the emphasis in this work⁴ was placed on comparison between the two discrete ordinates methods, multigroup and Streaming Ray, it represented a significant step in the development of the multigroup method as a practical means for performing electron transport calculations and obtaining physically meaningful quantities, such as energy deposition, which could later be used to predict dose profiles in metallized semiconductors, for example. An important reason for choosing the ONETRAN code to implement the multigroup discrete ordinates method is the fact that it employs the linear discontinuous spatial differencing scheme. This affords the advantage of accurate and stable flux convergence while requiring fewer spatial mesh cells that might have been necessary with the diamond difference approximation¹⁰ used in earlier discrete ordinates codes.

II.2.1.1 Scattering Model for Electrons

In this set of discrete ordinate calculations, the model assumed for electron scattering is given by the following expression for screened Rutherford elastic electron-nuclear scattering.

$$\sigma_s(T, \omega) = 2\pi \frac{Z}{A} (Z+1) N_A r_0^2 \left[\frac{T+1}{T(T+2)} \right]^2 \left[\frac{1}{(1+\eta-\omega)^2} \right], \quad (1)$$

where

- T = electron kinetic energy in mc² units,
- Z = atomic number of the transport medium,
- A = atomic weight of the transport medium,
- N_A = Avogadro's number,
- r₀ = e²/mc² (classical electron radius),
- η = atomic screening constant,
- ω = cosine of the scattering angle.

The units of the cross section are (cm²/g). The screening constant, η is given by the Moliere formula⁴,

$$\eta = 0.5 \left[\frac{Z^{1/3}}{.855(137)} \right]^2 \left[\frac{1}{T(T+2)} \right] \left[1.13 + 3.76 \left(\frac{Z}{137} \right)^2 \frac{(T+1)^2}{T(T+2)} \right] \quad (2)$$

The anisotropy of the scattering cross section angular dependence increases with electron energy. This causes problems such as numerical instability and slow convergence in discrete ordinates calculations. Because the magnitude of the single scattering electron deflection is small, an impractically large number of discrete ordinates would be required to adequately describe the angular dependence of the flux and scattering cross section. This difficulty was circumvented by the use of the extended transport corrected cross section¹¹. This approach can be described in brief terms as having the effect of separating out the delta function (in angle) component for the scattering cross section, leaving behind a more manageable (weak anisotropy) angular behavior for the cross section. The extended transport correction of order L is defined in terms of the Legendre series coefficients, $\sigma_L(E)$, of the scattering cross section in the following way:

letting

$$\sigma_s(E; \mu, \mu') = \sum_{\ell=0}^{\infty} (\ell + \frac{1}{2}) \sigma_{\ell}(E) P_{\ell}(\mu) P_{\ell}(\mu'), \quad (3)$$

where μ, μ' = cosines of the electron polar obliquities (slab geometry) before and after scattering, respectively,

$\sigma_{\ell}(E)$ = Legendre series coefficients of the scattering cross section,

P_{ℓ} = Legendre polynomial of order ℓ .

The extended transport corrected cross section for an L-th order correction is given by

$$\sigma_s^*(E; \mu, \mu') = \sum_{\ell=0}^L (\ell + \frac{1}{2}) \sigma_{\ell}^*(E) P_{\ell}(\mu) P_{\ell}(\mu'), \quad (4)$$

where

$$\sigma_t^*(E) \equiv \sigma_t(E) - \sigma_l(E). \quad (5)$$

II.2.1.2 Energy Group Structure

In the multigroup calculations the energy domain of interest was partitioned into a number of equal width energy groups, with the upper bound of the highest energy group defined as the source energy. The lower bound of the lowest energy group was taken to be a few eV above the mean ionization potential for the scattering material. The group-to-group transfer cross sections were determined using the continuous slowing-down approximation. Because of the absence of up-scatter terms under this assumption, and the fact that down-scatter can occur only between adjacent groups, only one iteration on the energy groups was required. For group g , with midpoint energy E_g , the cross section for scatter into group $g+1$ ($E_g > E_{g+1}$) is given by

$$\sigma_{g,g+1} = \frac{1}{\Delta E_g} \left| \frac{dE}{ds} \right|_{E_g}, \quad (6)$$

where dE/ds = collision stopping power,
and ΔE_g = width of energy group g .

The collision stopping power accounts for the energy lost by the incident electron to bound atomic electrons. The Berger-Seltzer stopping power formula^{1,2} was used to calculate dE/ds .

II.2.1.3 Target and Source Geometries

The monodirectional electron source was assumed incident on the left face of the scattering medium (Fig.1). Since ONETRAN contains no provision for a monodirectional edge source, and since a Legendre series is not a practical means for representing a delta function in angle, the unscattered monodirectional source was replaced by a spatially distributed source for once-scattered electrons. The expression for this is given by

$$Q_1(x, \mu) = e^{-\sigma_0^* x / \mu} \sum_{l=0}^{\infty} \left(l + \frac{1}{2} \right) \sigma_t^*(E_0) P_l(\mu) P_l(\mu_0), \quad (7)$$

where

$Q_1(x, \mu)$ = source function for once-scattered electrons,

x = distance into slab along the direction normal to the slab surface (Fig.1),

and μ_0 = cosine of the source angle of incidence w.r.t. slab normal.

II.2.1.4 Energy Deposition Calculation

Energy deposition profiles in an aluminum slab due to the incidence of a 200 keV electron source were obtained with the group flux values, $\Phi_g(x)$, calculated with ONETRAN. In terms of the group fluxes, the electron energy deposition profile was calculated as the sum of the scattered and direct contributions as follows;

$$W_D(x) \approx \sum_{g=1}^G \Phi_g(x) \left| \frac{dE}{ds} \right|_{E_g} + \Phi_0(x) \left| \frac{dE}{ds} \right|_{E_0}, \quad [8]$$

where E_g is taken as the group midpoint energy, G is the total number of groups used in the calculation, and Φ_0 is the unscattered flux. The energy deposition function was calculated at N points, x_n , where N is the number of spatial mesh cells used in the calculation, and x_n is the value of x at the center of the n -th cell, the approximate position of the cell-averaged flux. The cell-averaged unscattered flux contribution Φ_0 was calculated as

$$\begin{aligned} \Phi_0^n &= \frac{1}{\Delta x_{n-1}} \int_{-1}^1 d\mu \int_{x_{n-1/2}}^{x_{n+1/2}} dx \exp[-\sigma_0^*(E_0)x/\mu] \delta(\mu - \mu_0) \\ &= \frac{\mu_0}{\sigma_0^*(E_0)\Delta x_n} \left[\Phi_0^{n-1/2} - \Phi_0^{n+1/2} \right], \end{aligned} \quad [9]$$

where the $\Phi_0^{n+1/2}$ and the $x_{n+1/2}$ are respectively defined as the scalar edge fluxes and coordinates for the n -th cell edges, and

$$\Delta x_n \equiv x_{n+\frac{1}{2}} - x_{n-\frac{1}{2}}. \quad [10]$$

Then, for the n -th cell,

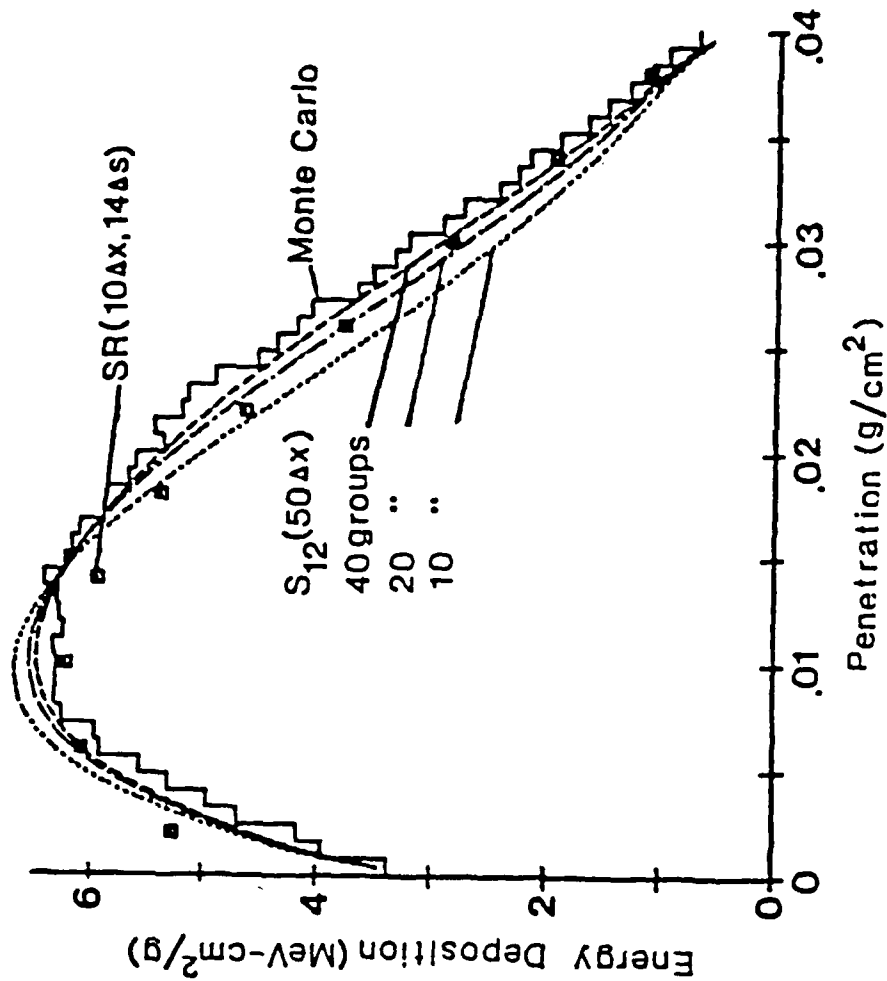


Figure 2. Energy Deposition Profile for 0.2 MeV electrons obliquely incident ($\mu_0 = .916667$) on an aluminum slab of thickness 0.04 g/cm² (Ref.4).

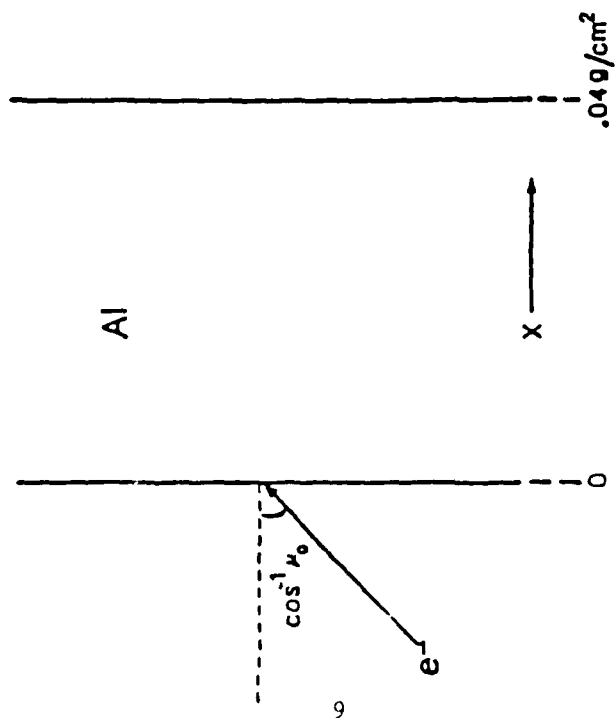


Figure 1. Problem Geometry (Ref.4).

$$W_D^n = \sum_{g=1}^G \phi_g^n \left| \frac{dE}{ds} \right|_{E_g} + \frac{\mu_o}{\sigma_o(E_o) \Delta x_n} \left[\phi_o^{n-\frac{1}{2}} - \phi_o^{n+\frac{1}{2}} \right] \left| \frac{dE}{ds} \right|_{E_g} \quad (11)$$

II.2.1.5 Energy Deposition Profile Results

Three ONETRAN calculations, 10, 20 and 40 groups, were made for a monodirectional electron source of incident obliquity $\mu_o = .916667$. The energy deposition profiles were compared with Streaming Ray calculations and a 10000 case history TIGER Monte Carlo calculation. The resulting energy deposition profile data are shown in Fig. 2. The three curves in the figure correspond to the three ONETRAN calculations in which the spatial grid was divided into 50 mesh intervals. The Streaming Ray calculation was configured with 10 and 14 spatial (Δx) and path length (Δs) mesh intervals, respectively. The histogram represents the Monte Carlo result. Overall agreement among the three methods of calculation is very good. The agreement between the ONETRAN and the Monte Carlo calculations improved as the number of energy groups was increased. Also, if the coarseness of the Streaming Ray calculation is taken into account, the agreement between the two discrete ordinates methods is satisfactory.

II.2.1.6 Transmission Energy Spectrum Results

Five ONETRAN S_{12} calculations (10, 20, 40, 60 and 80 groups) were made for the above source configuration. The aluminum slab thickness was taken to be 0.02 g/cm². In this way the effect of the number of energy groups on the artificial energy straggling problem could be observed. Streaming ray and Monte Carlo calculations were also made for the purpose of comparison. The TIGER Monte Carlo calculation was made with the straggling option turned on. That is, the energy loss fluctuations due to ionization were taken into account by the TIGER calculation. Figure 3 is a plot of the transmitted electron current per unit energy as calculated by the three methods. The Streaming Ray calculation was made with a coarse mesh, 4 and 11 spatial and path length mesh intervals, respectively. Also shown in this figure is the high energy cut-off (148.8 keV), the highest possible energy with which an electron can be transmitted through the slab under the continuous slowing-down approximation.

If no straggling, artificial or genuine, were present in any of these calculations, none of the transmitted electrons obtained with any of the three calculation methods would have energies

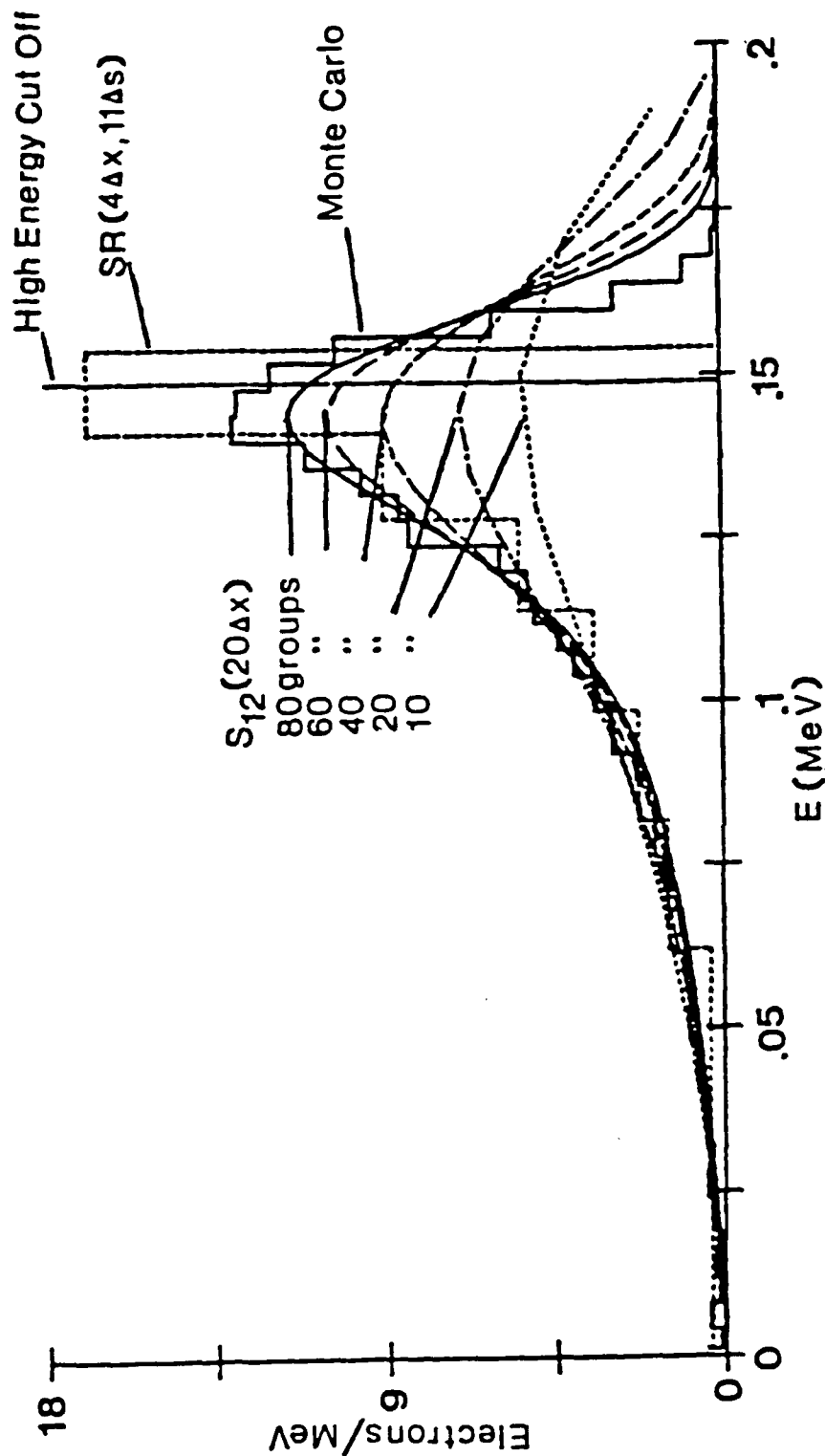


Figure 3. Transmitted Electron Current per unit energy per incident electron for 0.2 MeV electrons obliquely incident ($\mu_0 = .916667$) on aluminum slab of thickness 0.02 g/cm² (Ref. 4).

exceeding this value. As the number of energy groups in the ONETRAN calculation is increased, it can be seen that the numerical straggling problem is mitigated but not eliminated. Although it was found that numerical straggling could be virtually eliminated by the use of higher resolution Streaming Ray calculations, subsequent S_N studies with as many as 120 groups have indicated that further improvement in this regard is possible.

The versatility afforded by the S_N method, in particular the multiple slab capability, combined with the capability to calculate energy deposition, as shown in Fig.2, strongly suggest that ONETRAN-type discrete ordinates calculations will be very useful for the prediction of ionizing radiation effects in materials.

II.2.2 Plane Electron Sources Embedded in an Infinite Medium⁶

Since it has been an intention of the research and development activity of this contract to produce a working, reliable discrete ordinates electron transport code, it was and is necessary to compare the results of our discrete ordinates calculations with known benchmark solutions of electron transport problems as is possible and practical. The following is a report of benchmark comparisons we have made. As in the work reported in the previous section, another discrete ordinates method in addition to the S_N method was employed, the Streaming Ray method. Benchmark data were obtained from two sources, the method of moments⁹, for energy deposition data, and, for flux values, an analytical benchmark solution of the Spencer-Lewis equation⁴.

II.2.2.1 Plane Perpendicular Source - Electron Energy Deposition in Aluminum

Discrete ordinates methods were applied to the transport of electrons emanating from a plane perpendicular source embedded in a "thick", or infinite medium. Choice of this problem configuration was motivated by the existence (since 1959) of extensive published data⁹ calculated by Spencer using flux moments reconstruction. Both the ONETRAN S_N and Streaming Ray methods were applied to this problem. The second method served as yet another independent check on the validity of the ONETRAN approach.

The first extensive theoretical study of electron transport and energy deposition in infinite media was made by Spencer⁹. In this work the method of moments was applied to obtain the energy deposition profile from plane perpendicular and point isotropic sources. Calculations of the energy deposition function by moments reconstruction were performed for five elements, air and polystyrene, for electron energies ranging from 0.025 to 10.0

MeV. Extensive tabulations of the energy deposition profile are given for both source configurations. This moments data serves as a standard, since as far as is known, it most closely represents numerical solutions of the Spencer-Lewis equation⁴.

The problem chosen for comparison of the discrete ordinates methods with the moments data was that of a 200 keV plane perpendicular source, located at $x=0$, in "infinite" (>1 electron range in both positive and negative directions) aluminum. The results of the ONETRAN discrete ordinates calculations are shown in comparison with the moments curve, obtained from the data of Ref. 9., in Fig.4. The solid curve is the moments result, while the dashed curves are the ONETRAN S_N results for two cases, 40 and 100 uniformly spaced electron energy groups. In the S_N calculations, 47 spatial grid intervals were used with three coarse mesh zones. The zone of highest resolution enclosed the source plane ($x=0$). The multigroup electron scattering cross sections and stopping power values were obtained with a shortened version of DATAPAC², a computer code for calculating electron stopping powers, ranges and Mott scattering cross sections. The S_N calculations were performed using P_{12} extended transport corrected Mott cross sections. The apparently slight effect of numerical straggling due to energy discretization is somewhat mitigated by increasing the number of energy groups, the only difference between the two S_N calculations. As can be seen, the 40 and 100 groups curves are nearly indistinguishable from one another, and their agreement with the moments curve is very good. The effect of artificial or numerical diffusion near the source plane due to discretization of the spatial variable, x , was in all likelihood reduced by the use of the high resolution spatial grid about the source plane. In addition to the accuracy of the linear discontinuous spatial differencing scheme, the capability of varying the spatial grid resolution in this manner is one of the principal advantages afforded by the ONETRAN code.

Figure 5 shows a comparison of energy deposition results obtained with both the ONETRAN- S_N (100 group) and the Streaming Ray methods with the moments reconstruction curve. The Streaming Ray calculation was done with 72 and 36 spatial(Δx) and path length(Δs) mesh intervals, respectively. Agreement among the three methods is very good. While some oscillation is observable in the left tail of the moments curve, it is probably attributable to truncation error introduced by Spencer's finite approximation (10 terms) to an infinite series.

II.2.2.2 Comparison of Discrete Ordinates Flux Calculations with An Analytical Benchmark Solution of the Spencer-Lewis Equation

The foregoing discussion dealt with the comparison of discrete ordinates and moments calculations of energy deposition,

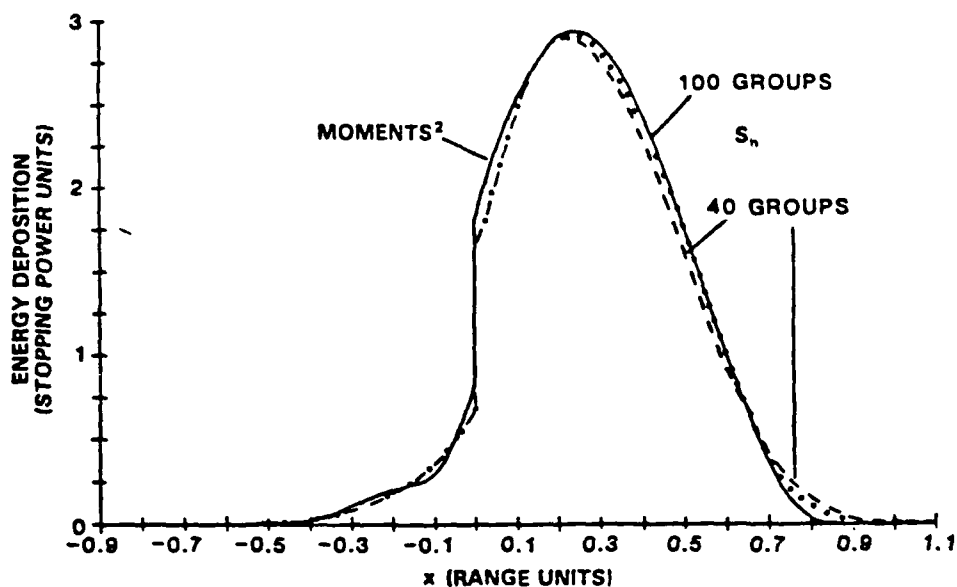


Figure 4. Energy deposition profile for a 200 keV plane perpendicular electron source ($x=0.0$) in aluminum obtained with S_n and moments calculations (Ref.6).

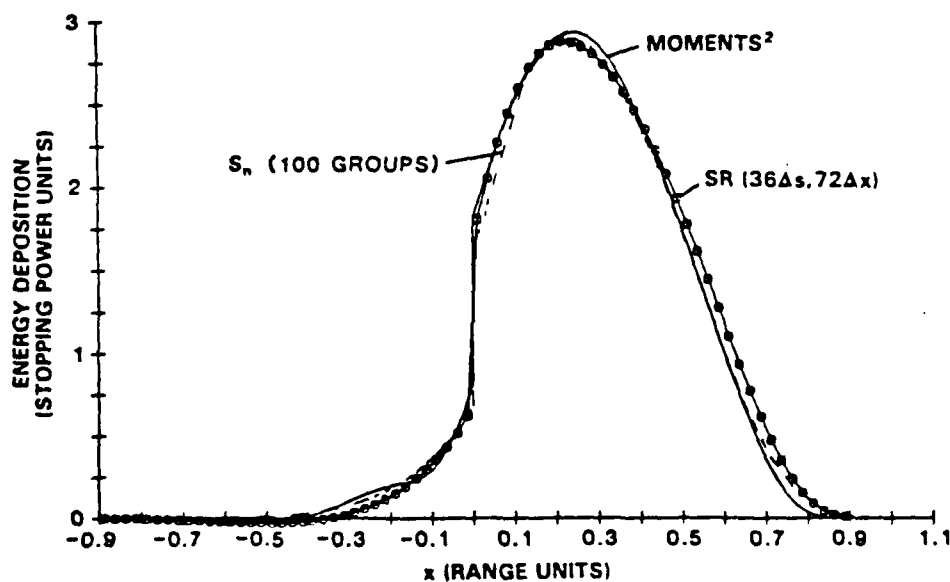


Figure 5. Energy deposition profile for a 200 keV plane perpendicular electron source ($x=0.0$) in aluminum obtained with S_n , Streaming Ray, and moments calculations (Ref.6).

which is of fundamental significance in the analysis of x- and gamma-radiation effects in semiconductor materials. Of no less importance, however, in the development of discrete ordinates electron transport methods is that of making comparisons with analytical solutions. Generally, validation of a flux calculation is a more demanding test of the accuracy of the discrete ordinates method than that of an energy deposition calculation. This follows from the fact that the energy deposition is an integral quantity (for example, see Eq. 8 of section II.2.1.4) so that inaccuracies in the terms of the integrand, flux for example, can become obscured either by error cancellation or by the possibility that the largest errors may occur in the smallest terms. For this reason, Ref. 6 also presents extensive comparisons of flux calculated by ONETRAN-S_N and Streaming Ray discrete ordinates methods with an analytical benchmark solution, based on polynomial reconstruction, to the constant parameter Spencer-Lewis equation for scattering in an infinite medium.¹³

Some restrictive assumptions were made in order to perform the analytical benchmark calculations, however these in no way altered the validity of the benchmarking procedure, since these same restrictions could be applied to the discrete ordinates calculations. A screened-Rutherford scattering cross section⁴ was used. The screening parameter, η (defined in Ref. 4) for this kernel was assumed to be constant and independent of electron energy. This was done in order to make use of a multiple collision expansion which greatly simplified the analytical calculation.

Two test problems were devised using the analytical benchmark technique¹³ to assess the accuracy of the discrete ordinates numerical algorithms. The test problems treated a plane electron source located at the center of an infinite medium emitting source particles of zero path length either isotropically or in direction $\mu_0 = 1$. Two values of the screening parameter were assumed, $\eta = 1.0, 0.01$. The scattering kernel was taken to be an order 12 extended transport corrected Legendre expansion of the screened-Rutherford scattering function.

Figures 6-11 are plots of the scalar flux, $f(x,s)$ vs. x for plane sources embedded in infinite media, infinite in the sense that the fluxes given are shown only for distances less than the electron path length, s (all distances and path lengths are measured in units of total mean free path). The order of the plots is given in Table 1. It can be seen that the discrete ordinates results are in overall agreement with the benchmark curves. The ONETRAN-S_N values diverge from the benchmark case to a greater extent than do the Streaming Ray values in the wave front region (where x approaches s). It is in this region where the numerical diffusion characteristic of S_N, i.e. spill-over

Table 1.
Description of Scalar Flux Plots (Figs.6 through 11) (Ref.6)

Figure	Source	Screening Parameter η	Discrete Ordinates Mesh Configuration				Path Length Values s (mfp)
			SR		S_0		
			Δs	Δx	Number of Groups	Δx	
6	Plane isotropic	1.0	20	20	20	20	9.5 and 18.5
7	Plane isotropic	1.0	40	40	40	40	9.25 and 18.25
8	Plane isotropic	0.01	20	20	20	20	9.5 and 18.5
9	Plane isotropic	0.01	40	40	40	40	9.25 and 18.25
10	Plane perpendicular	1.0	20	20	20	20	9.5 and 18.5
11	Plane perpendicular	1.0	40	40	40	40	9.25 and 18.25

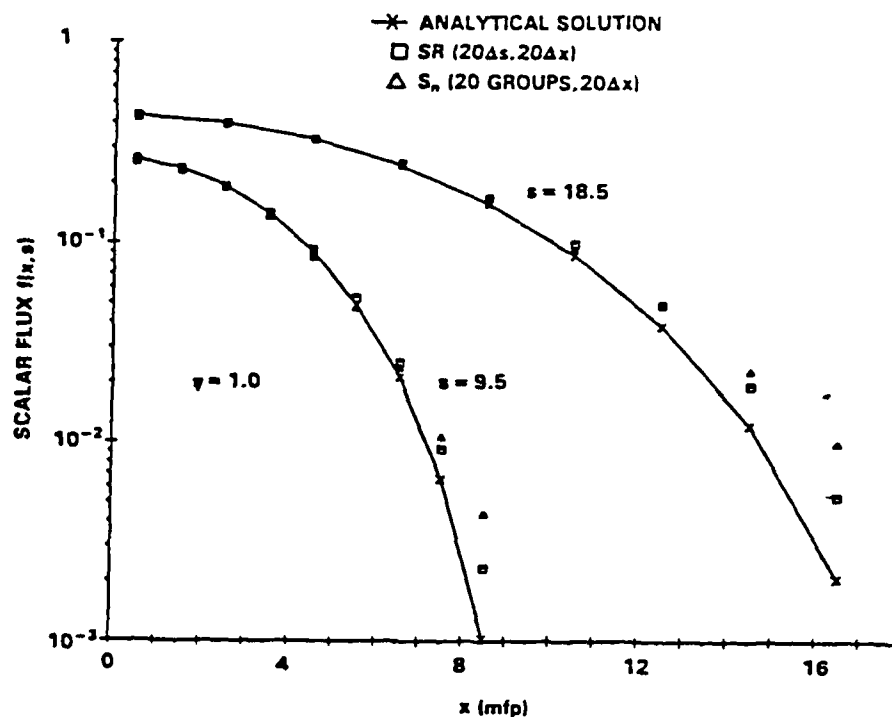


Figure 6. Comparison of scalar flux results, $f(x,s)$ vs. x for two s values, 9.5 and 18.5 mfp, calculated using the analytical benchmark algorithm, S_n (20 groups, 20 Δx) and Streaming Ray (20 Δs , 20 Δx) discrete ordinates methods. Plane isotropic source at $x=0.0$. Screened-Rutherford scattering $\eta=1.0$ (Ref.6).

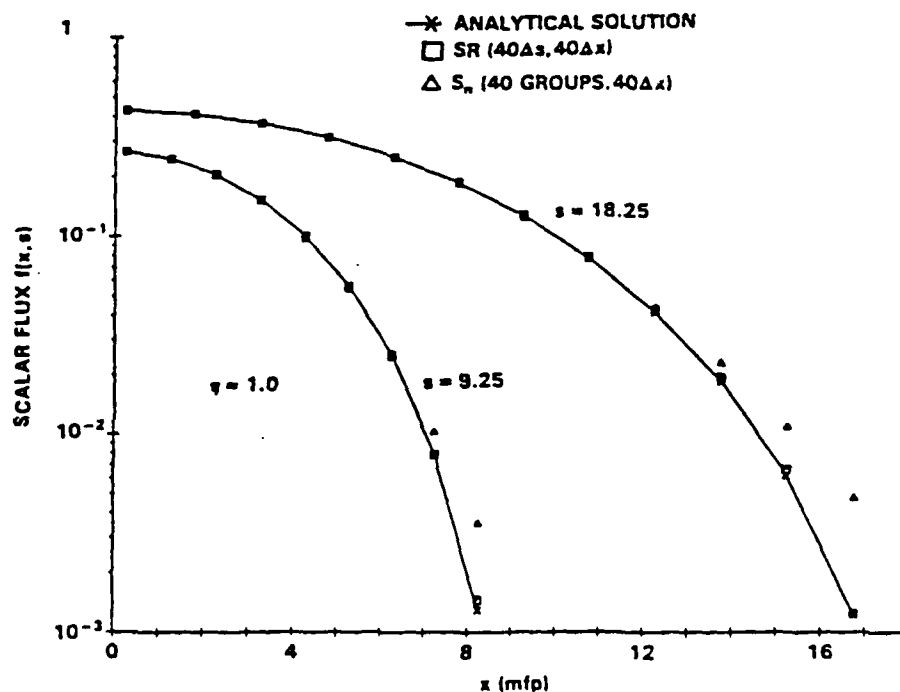


Figure 7. Scalar flux. Source configuration and η value as in Fig.6, but for S_n (40 groups, 40 Δx) and Streaming Ray (40 Δs , 40 Δx) calculations at $s=9.25$ and 18.25 (Ref.6).

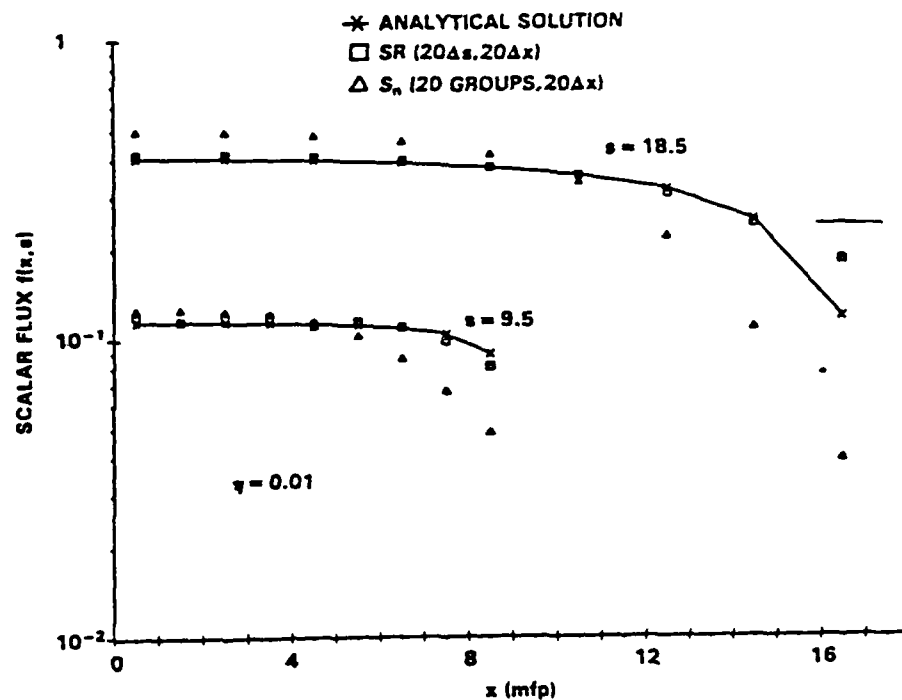


Figure 8. Comparison of scalar flux results, $f(x,s)$ vs. x for two s values, 9.5 and 18.5 mfp, calculated using the analytical benchmark algorithm, S_n (20 groups, $20 \Delta x$) and Streaming Ray ($20 \Delta s, 20 \Delta x$) discrete ordinates methods. Plane isotropic source at $x=0.0$. Screened-Rutherford scattering $\eta=0.01$ (Ref.6).

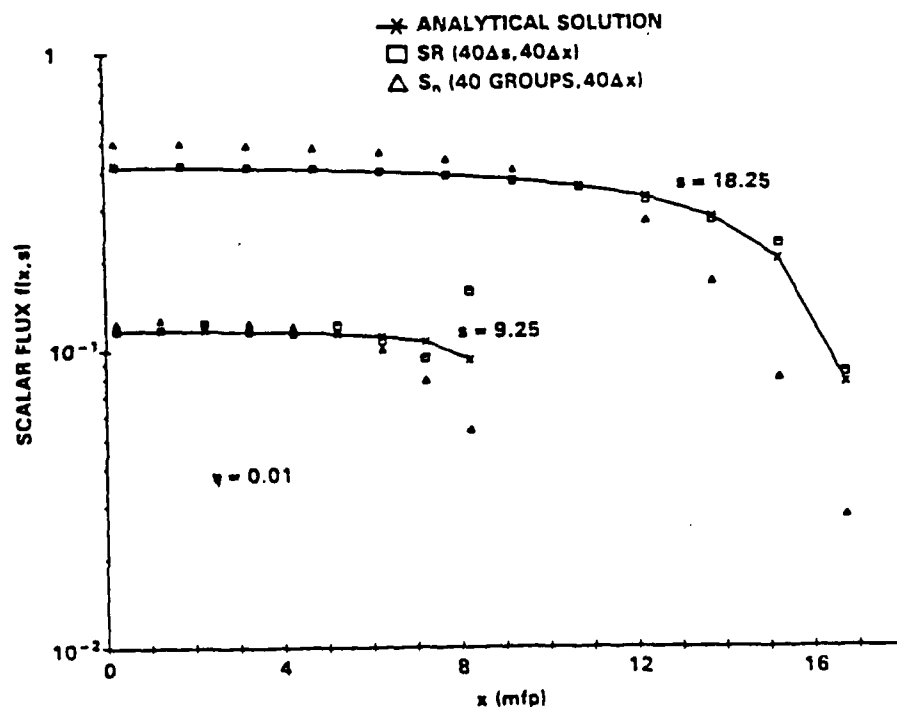


Figure 9. Scalar flux. Source configuration and η value as in Fig.8, but for S_n (40 groups, $40 \Delta x$) and Streaming Ray ($40 \Delta s, 40 \Delta x$) calculations at $s=9.25$ and 18.25 (Ref.6).

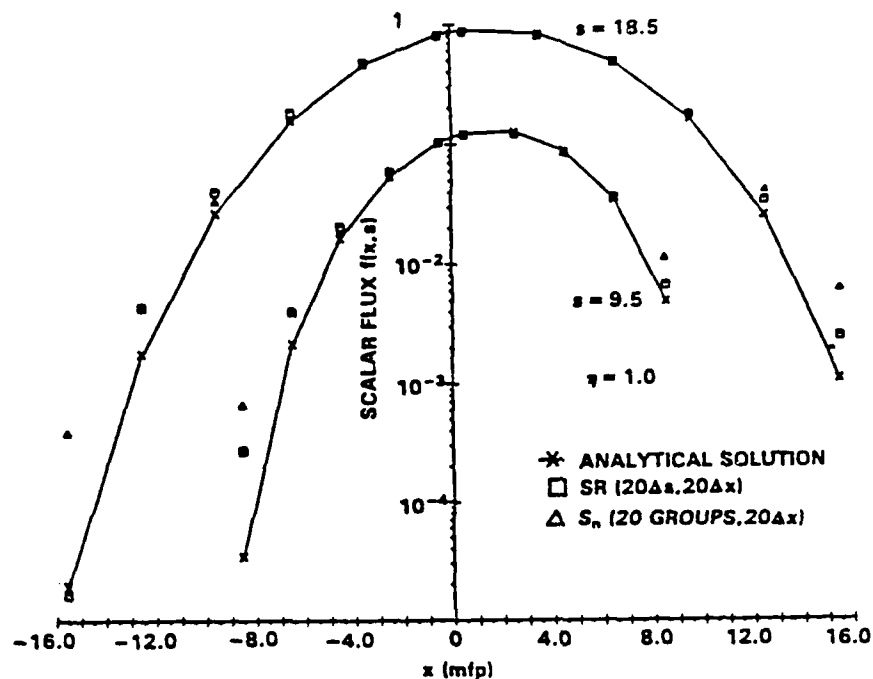


Figure 10. Comparison of scalar flux results, $f(x,s)$ vs. x for two s values, 9.5 and 18.5 mfp, calculated using the analytical benchmark algorithm, S_n (20 groups, $20\Delta x$) and Streaming Ray ($20\Delta s, 20\Delta x$) discrete ordinates methods. Plane perpendicular source at $x=0.0$. Screened-Rutherford scattering $\eta=1.0$ (Ref.6).

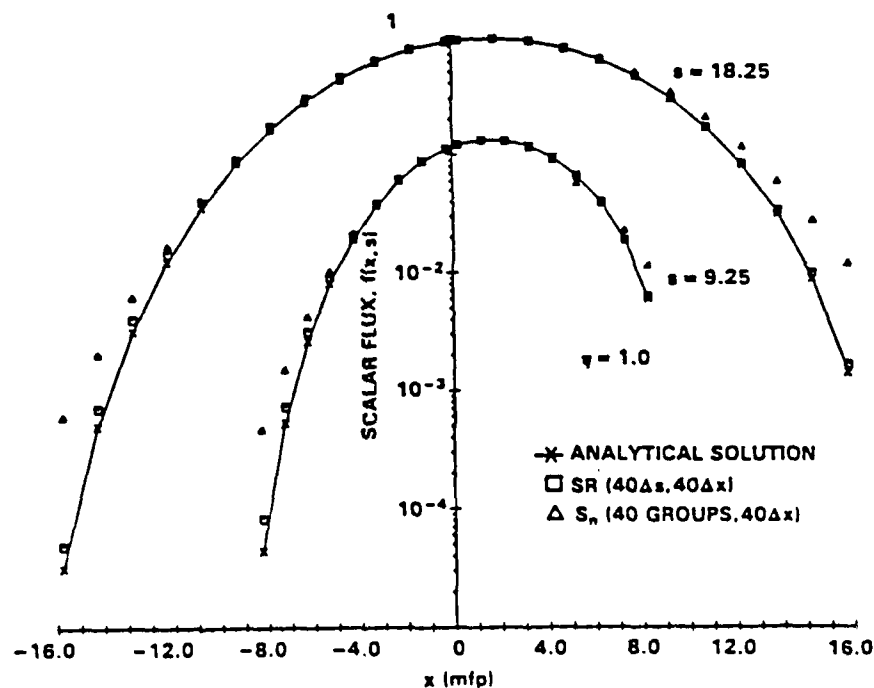


Figure 11. Scalar flux. Source configuration and η value as in Fig.10, but for S_n (40 groups, $40\Delta x$) and Streaming Ray ($40\Delta s, 40\Delta x$) calculations at $s=9.25$ and 18.25 (Ref.6).

into the forbidden region ($x > s$), causes problems. This problem is also present in the Streaming Ray calculation.

Numerical diffusion due to spatial discretization error is evidenced in the S_N results not only in the wave front region for both the $\eta=1.0$ (Figs.6,7,10,11) and $\eta=0.01$ (Figs.8,9) cases, but also near the source plane in the $\eta=0.01$, plane isotropic source case (Figs.8,9). Diffusion can be regarded as the migration of particles from regions of higher density to regions of lower density. The results here are consistent with this view. In the nearly isotropic scattering cases (Figs.6,7,10,11) where $\eta=1.0$, the S_N flux values are well above the benchmark case as x approaches s . The electrons diffuse gradually from the center to the wave front, where the particle density is low, and remain there, since there is no sharp decrease in particle density as the wave front is approached. In the more forward peaked scattering case (Figs.8,9), where $\eta=0.01$, the S_N results again exhibit electron diffusion toward the wave front region. However, because there is a large flux gradient at the wave front, the artificial diffusion into the forbidden region ($x > s$) is more pronounced, and the result is lower S_N flux values as x approaches s .

The work discussed here further illustrates that the method of discrete ordinates, in particular our version of the ONETRAN code, can be used to obtain solution to physically realistic problems in electron transport, the 200 keV plane perpendicular electron source in Aluminum, for example. These calculations agree well with Spencer's moments results, which in turn, agree well with experiment. The comparisons with analytical benchmark calculations are also useful in that we are afforded a quantitative measure of the limitations of the method of discrete ordinates. It is reassuring to note that the method of discrete ordinates can calculate electron flux accurately. However, detailed knowledge of where the numerical (or artificial) diffusion causes inaccuracies is valuable and serves as a reminder that close agreement of ONETRAN calculations with experiment or other computational techniques, such as Monte Carlo, can on occasion be fortuitous, particularly when the numerical straggling of the discrete ordinates calculation approximates physical straggling.

II.3 Determination of Electron and Gamma Ray Induced Dose Enhancement and Atomic Displacement Damage in Gallium Arsenide and Silicon⁸

The method of discrete ordinates was applied to obtain dose profiles, electron flux spectra and displacement damage rate profiles in GaAs and Si for incident electron beams and gamma rays. For these calculations, the ONETRAN code was used, in conjunction with two programs, FRONT, a processor program to convert electron beam and photon source data into ONETRAN-compatible input, and ESRCE, a program to calculate the secondary electron distribution in target materials due to incident gamma radiation (the programs FRONT and ESRCE will be described in section II 6). The work to be described here provides a clear example of practical applications of the discrete ordinates electron transport calculation method. As will be seen here, one of the principal advantages of the discrete ordinates method is the ability to calculate electron flux energy spectra as a function of position inside the target medium, generally with higher accuracy and more detail than is available with other methods, Monte Carlo for example. Because of this, it was possible to obtain displacement rate profiles, as well as dose profiles, inside the target materials, and to study their variation with source type (electron or gamma ray), energy and incident direction. In addition to displacement rate profiles obtained for electron beams incident on GaAs and Si, both displacement rate and dose profiles were calculated for gamma radiation incident on Au/GaAs and Au/Si.

The dose enhancement effect in x- or gamma irradiated materials of low atomic number (such as silicon) next to high atomic number materials (such as gold) is well studied and has been discussed in many papers^{15, 16}. The energy deposited at and near the high z-low z interface can be larger than the equilibrium dose by more than a factor of 10. The maximum effect, an enhancement factor of 30 is obtained in silicon at the gold-silicon boundary for 150 keV photons incident on the silicon side. Recent interest in the radiation hardness properties of GaAs provided some of the motivation for the study of dose enhancement effects in this material as well.

II.3.1 Electron Flux Energy Spectra in GaAs and Si

Electron flux energy spectra were calculated at various positions in GaAs and Si for both electron beam and gamma ray sources. These spectra are shown for a 1.2 MeV electron beam normally incident on GaAs and Si are shown in Figs. 12 and 13. Four curves are shown in each graph, corresponding to four beam penetration distances (.05, .1, .15, .2 and .1, .2, .3, .4 electron range units for GaAs and Si, respectively). It can be seen in both cases that as the distance into the medium is

increased, the energy spectra shift toward lower energy values. Solution of the transport equation through the ONETRAN discrete ordinates code enabled the calculation of these flux spectrum curves. If the Monte Carlo method were used instead of the method of discrete ordinates, smooth curves such as shown here would not be obtainable under normal circumstances due to the stochastic nature of the method. It is the availability of energy spectrum curves such as these which made possible the calculation of dose and displacement damage rates at arbitrary positions within the target material.

The energy flux spectra of electrons due to the incidence of 1.25 MeV gamma-rays on Au/GaAs and Au/Si are shown in Figs.14 and 15, respectively. The energy spectra at three positions are plotted in each graph: 1) the spectrum at an equilibrium position in GaAs or Si (i.e. the position at which the boundaries, vacuum and material, are greater than one electron range away); 2) the flux spectrum at the material interface due to gamma-rays incident from the Au side; 3) the flux spectrum at the material interface due to gamma-rays incident from the GaAs or Si side.

II.3.2 Energy Deposition and Displacement Calculations

II.3.2.1 Electron Beam Induced Profiles

Given the electron flux energy spectrum, $\Phi(E,x)$, where E denotes energy and x denotes the position in the target slab, both the energy deposition and displacement damage rate profiles can be readily calculated. For energy deposition, $D(x)$, the expression is

$$D(x) = \int_0^{E_{\max}} \Phi(E,x) \frac{dE}{ds} dE, \quad (12)$$

where, as before, dE/ds is the electron stopping power.

Displacement rate, $R(x)$, is calculated as

$$R(x) = \int_0^{E_{\max}} \Phi(E,x) \sigma(E) dE, \quad (13)$$

where $\sigma(E)$ is the displacement cross section.

The displacement cross section, $\sigma(E)$, was calculated by performing numerical integrations over angle of the Mott differential cross sections^{2,17} for Si and GaAs. Fig.16 is a plot of the two displacement cross sections vs. electron energy. Fig.17 shows a comparison of the dose and displacement rate profiles for the 0.6 MeV electron beam incident on GaAs. As can

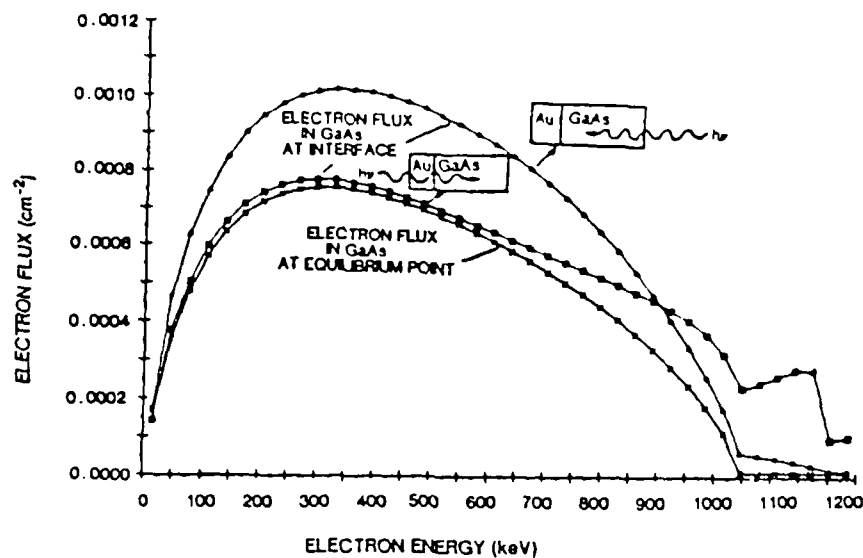


Figure 14. Electron flux energy spectrum in GaAs next to Au irradiated by 1.25 MeV gamma-rays (Ref.8).

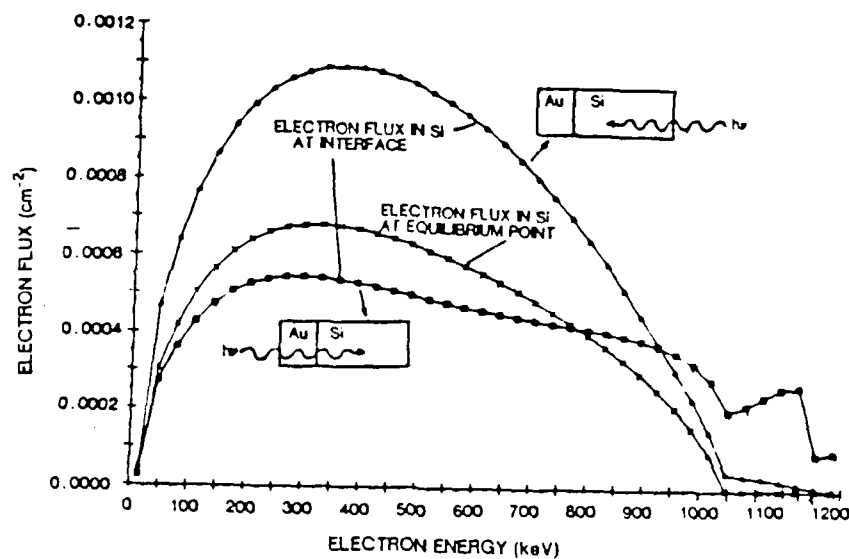


Figure 15. Electron flux energy spectrum in Si next to Au irradiated by 1.25 MeV gamma-rays (Ref.8).

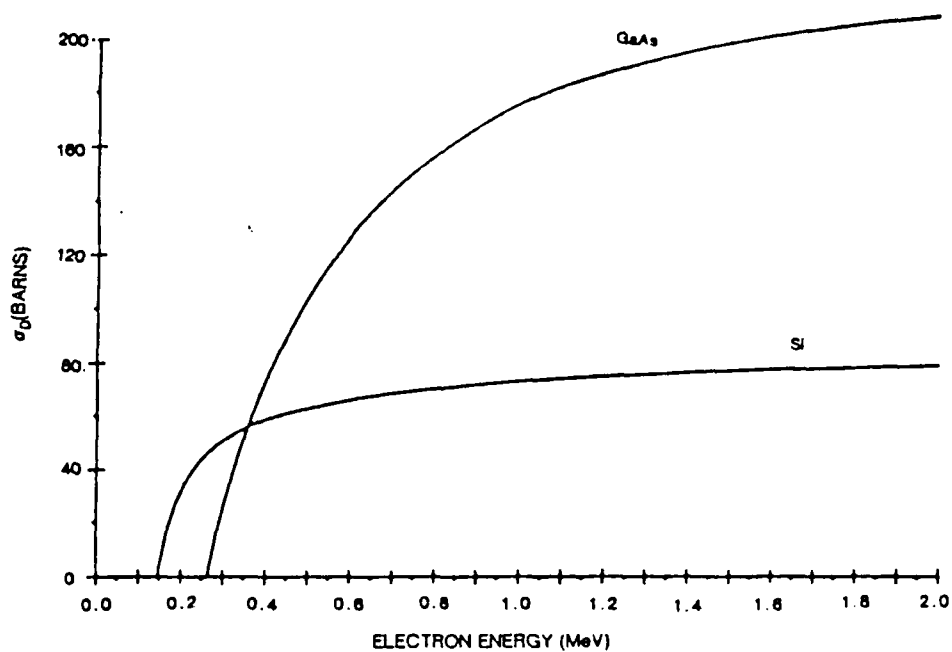


Figure 16. Displacement cross section vs. electron energy for GaAs and Si (Ref.8).

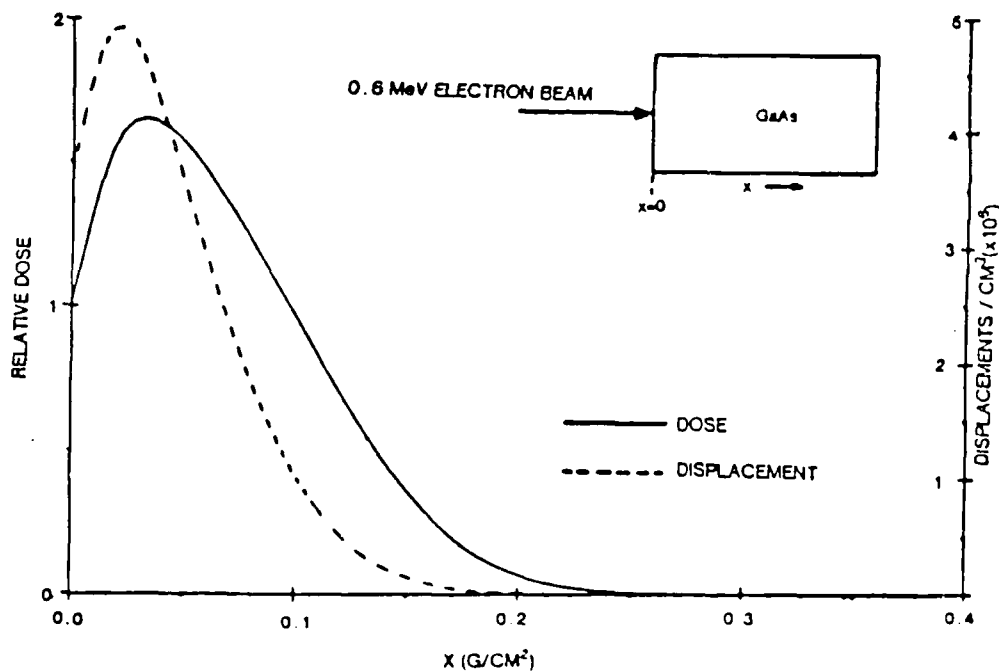


Figure 17. Relative dose and displacement rate profiles in GaAs due to a 0.6 MeV electron beam at normal incidence (Ref.8).

be seen, the displacement rate profile peaks sooner than the dose profile. This behavior is attributable to the rapid fall-off in the GaAs displacement cross section below 0.8 MeV coupled with the fact that the electron energy falls rapidly below 250 keV as the electron beam penetrates the medium. In the case of the dose profile, however, the low energy electrons (<250 keV) make a substantial contribution. In the 1.2 MeV incident beam case (not shown), the displacement rate and the dose profiles peak at about the same place. A similar set of results is given in Ref.8 for Si, along with a discussion of the differences between the two materials in this regard.

II.3.2.2 Gamma-ray Induced Profiles

The dose and displacement rate profiles in GaAs next to Au for 1.25 MeV gamma-rays normally incident on the Au and GaAs sides are shown in Figs.18 and 19, respectively. For gamma-radiation incident on the Au side, the dose enhancement effect in GaAs is small. The displacement rate profile shows an exponential-like decrease in accordance with the decrease with penetration distance of the gamma-induced electron flux. For gamma-radiation incident from the opposite direction, the dose and displacement rate profiles are nearly identical in shape. This is due to the fact that the shape of the electron flux energy spectrum does not vary much with position (see Fig.14). The rise in the dose and displacement damage curves in the interface region are also predictable from examination of the energy spectra of Fig.14.

As previously mentioned, further results and discussion are given in Ref.8. The most significant point to be made here is that the method of discrete ordinates, through the use of the ONETRAN transport code, provides an extensive and accurate (to within known limitations) knowledge of electron flux energy spectra. With these spectra one is enabled to calculate displacement damage and dose rate profiles in semiconducting materials.

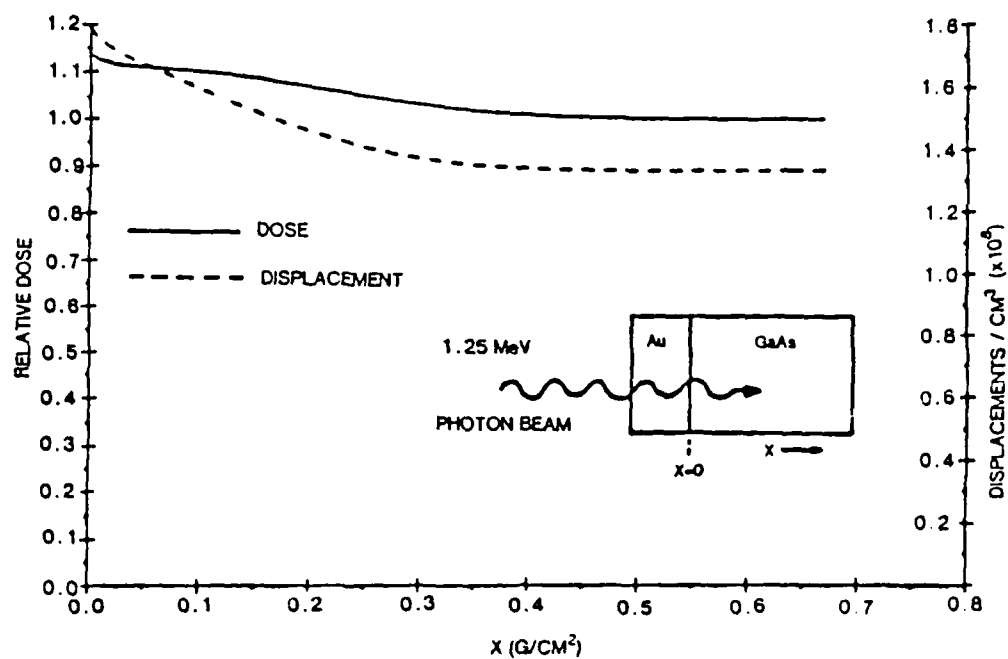


Figure 18. Relative dose and displacement rate profiles in GaAs next to Au due to 1.25 MeV photons approaching from the Au side (Ref.8).

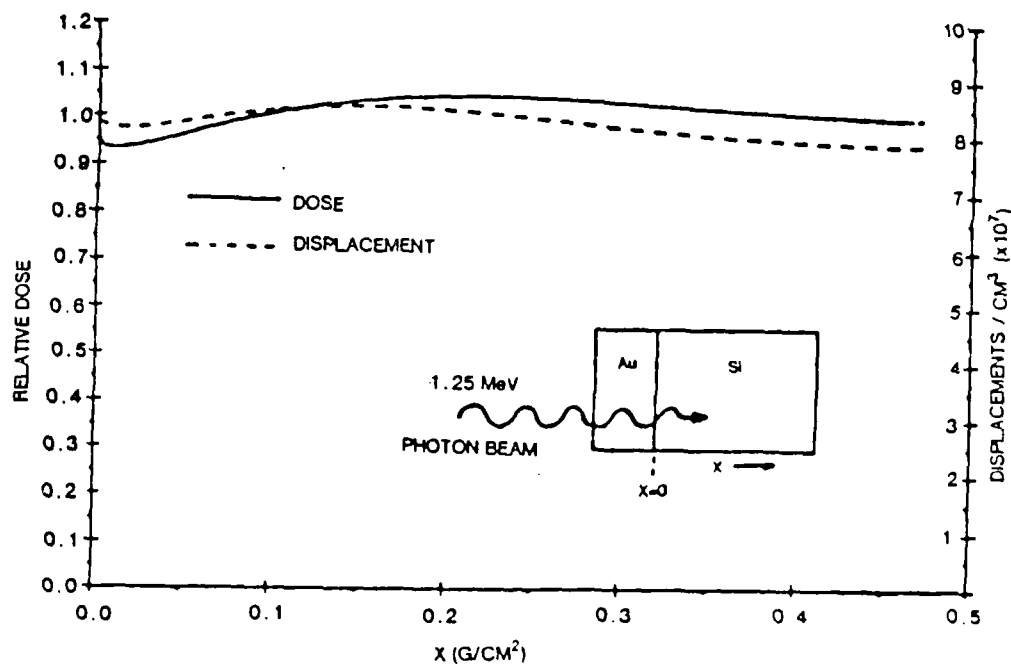


Figure 19. Relative dose and displacement rate profiles in Si next to Au due to 1.25 MeV photons approaching from the Au side (Ref.8).

II.4 Calculation of the Electron Flux Energy Spectrum Near a Two Medium Interface^{1,8}

The ONETRAN code was used to calculate the electron flux energy spectrum and dose profile as a function of distance from the interface between two semi-infinite media for a uniform isotropic source of electrons in one of the two media. The purpose of this work was to evaluate the accuracy of a simple analytic model^{1,9}, based on age-diffusion theory, derived by Garth, and to determine if this model, or a modified version of it, could provide a rapid, accurate algorithm for calculating energy spectra and dose.

Four cases of adjacent semi-infinite media were chosen for the computations, Al*/Al, Au*/Al, Al*/Au, and Au*/Au, where the (*) denotes the side containing the electron source. Four source energies were studied, 50, 100, 200 and 500 keV. Figure 20 is a plot of the electron flux energy spectrum in the all aluminum medium with a 50 keV half-space source on the left (Al*/Al) at 5 positions in the sourceless half, the interface and 0.05, 0.1, 0.2, 0.3 range units from the interface. The results are shown for the ONETRAN calculation and the age diffusion model. Both the ONETRAN and the age-diffusion models predict one-half the infinite medium continuous slowing down spectrum at the interface (slightly different shapes due to differences in stopping power models). As the distance from the interface is increased, it is found that the average electron energy as calculated by ONETRAN decreases more rapidly than that calculated by the age-diffusion model, while the total scalar flux decreases less rapidly, particularly at the larger distances from the interface.

In Figure 21 is shown a comparison of the electron flux energy spectra at the interface for the Al*/Au and Au*/Al configurations. While the age-diffusion model yields the continuous slowing down spectrum, the ONETRAN calculation shows a softened (relative to the age-diffusion case) spectrum for Al*/Au and a hardened spectrum for Au*/Al. The softening in the Al*/Au case reflects the fact that more low energy electrons are backscattered from the gold toward the interface than would otherwise be the case if the two semi-infinite media had been the same material (Al*/Al). Conversely, for the Au*/Al case, relatively fewer low energy electrons are backscattered from the aluminum toward the interface than if the materials on both sides of the interface had been gold (Au*/Au).

Differences between the discrete ordinates solution of the transport equation and the age-diffusion model are also apparent in the calculated dose profiles obtained by the two methods. Figure 22 shows the dose profile in Au*/Al as calculated by both. As was also apparent in Fig.21, penetration by electrons into the

medium on the right is deeper according to the transport equation model than as calculated by age-diffusion. The forward scattering of electrons is more rigorously treated by the ONETRAN calculation, hence the generally higher ONETRAN dose (Fig.22) and higher ONETRAN flux (Fig.21) in the medium on the right.

When the medium consists of only one material (i.e. Al^*/Al), the age-diffusion model agrees fairly well with the ONETRAN calculation. However, this is not the case for the two material medium such as Au^*/Al . The treatment of electron transport for the two material interface problem requires more rigor than is available with the age-diffusion model, but perhaps not quite as much as is provided by the full transport solution. For this reason, investigations into the applicability of an intermediate model were begun. Calculations, motivated by the apparent success of Shkurpelov et al.²⁰, were made with a P_2 solution of the Spencer-Lewis equation. This work is continuing at present.

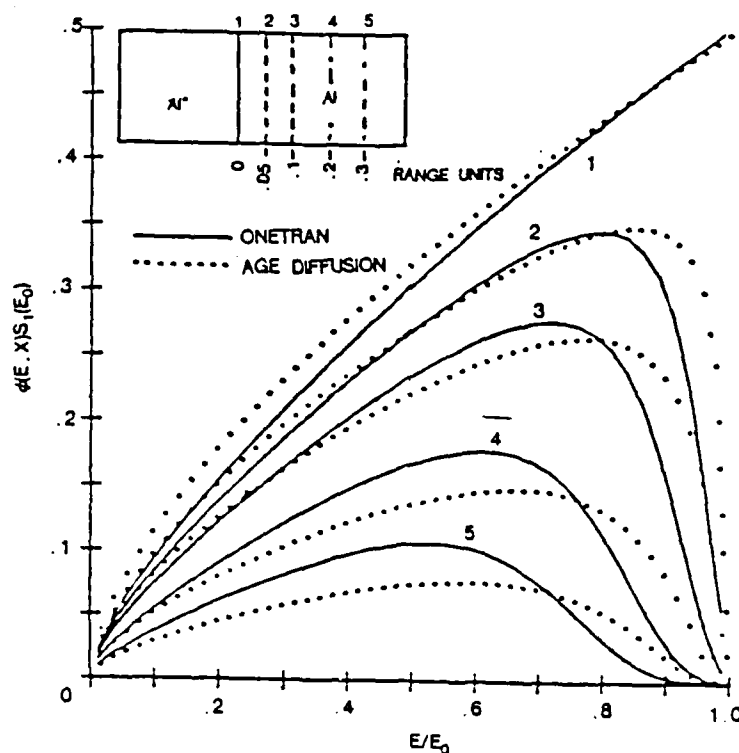


Figure 20. Electron flux energy spectrum in sourceless side of Al^*/Al medium with $E_0=50$ keV initial electron energy at (1)0, (2)0.05, (3)0.1, (4)0.2, and (5)0.3 range units from the interface (Ref.18).

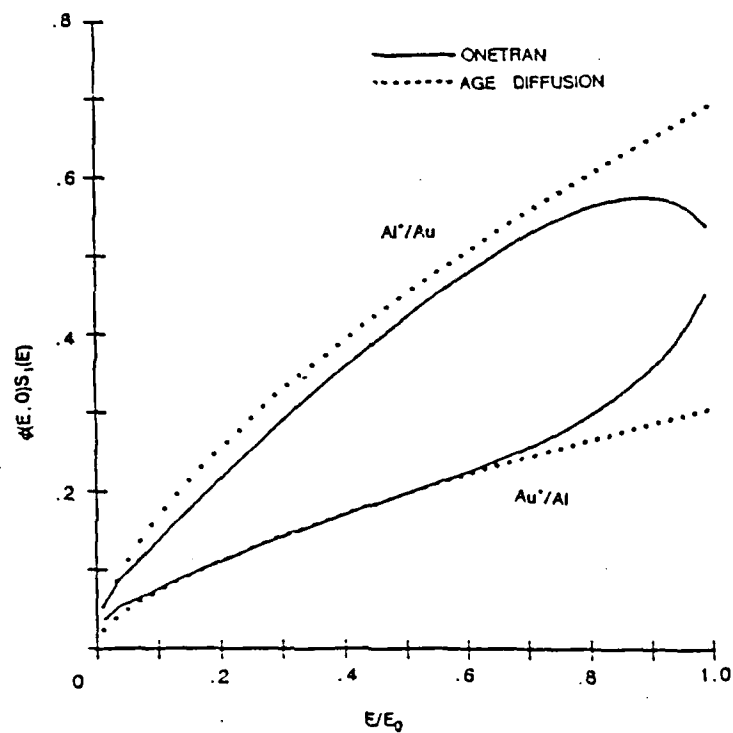


Figure 21. Electron flux energy spectrum at Al*/Au and Au*/Al interfaces with $E_0 = 50$ keV initial electron energy (Ref.18).

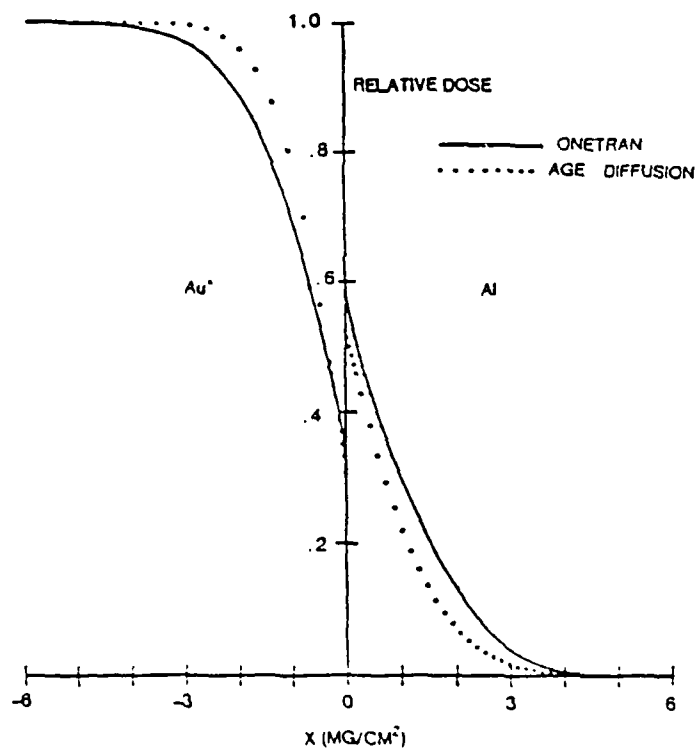


Figure 22. Dose profile on both sides of a Au*/Al interface with $E_0 = 50$ keV initial electron energy (Ref.18).

II.5 Determination of Scattered Cobalt-60 Photon Spectrum with ONETRAN Photon Dose Profile Calculations²¹

Results of ONETRAN calculations were used to "unfold" the Cobalt-60 scattered photon spectrum characteristic of an irradiation source used in a series of experiments reported in 1974 by Wall and Burke²². The series of dose profiles were computed with the ONETRAN code for 10 monoenergetic photon sources incident on layered media consisting of various combinations of Al, Au and C. The photon source energies were taken to be 100, 150, 200, 250, 300, 400, 600, 800, 1000 and 1250 keV. It was possible to combine some of the calculated dose profiles, according to a least-squares algorithm, to obtain a four component fit to the measured dose distribution data.

Application of the ONETRAN code to this problem involved the use of a computer program to generate electron sources from the Compton, photoelectric and Auger photon interactions. Our code, ESRCE, described briefly in section II.6, accomplishes this conversion with a procedure similar to that used in the POEM code²³. A series of ONETRAN calculations were made for gold/aluminum(Au/Al), aluminum/gold/aluminum(Al/Au/Al) and carbon/aluminum/gold(C/Al/Au) with the 10 photon energies listed above (see Fig.23). The photons were assumed normally incident. All material layers directly exposed to the source were assumed to be of equilibrium thickness. As shown in Fig.23, three gold thicknesses were assumed for the Al/Au/Al configuration, 25.4, 12.7 and 6.35 μ m. The thickness of aluminum in the C/Al/Au configuration was taken to be 275mg/cm².

The dose profile curves for the 10 photon source energies, as calculated by ONETRAN, for the Au/Al configuration are shown in Figs.24 and 25. The photons are assumed to be incident on the gold side in Fig.24 and on the aluminum side in Fig.25. These curves formed our set of "basis" functions for least-squares fitting of the experimental dose profiles of Wall and Burke²². A linear least-squares fitting procedure was devised to solve for the best linear combination of ONETRAN dose profile curves to correspond to the experimental data. The objective function, or the sum of the squares of residuals (difference between experimental and calculated values), to be minimized was taken to be

$$\left[\begin{array}{c} \text{Objective} \\ \text{Function} \end{array} \right] = \sum_{n=1}^N \left\{ F[x_n] - \sum_{j=1}^J a_j D_1[x_n, hv_j] \right\}^2 + \sum_{m=1}^M \left\{ B[x_m] - \sum_{j=1}^J a_j D_2[x_m, hv_j] \right\}^2, \quad (14)$$

where it is assumed that N dose measurements $F(x_n)$ are taken at

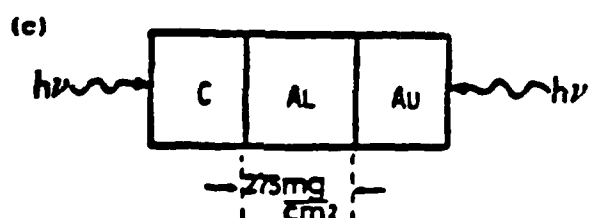
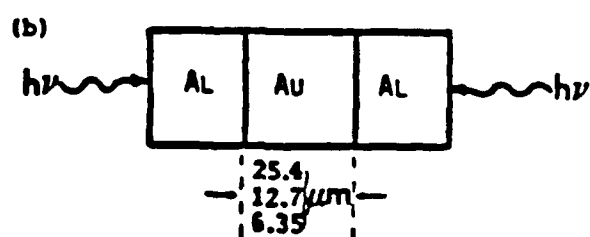
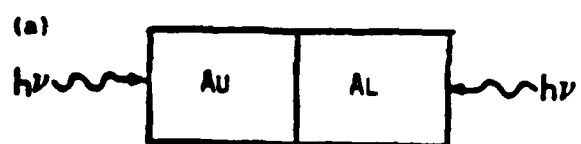


Figure 23. Interface geometries for: (a) gold-aluminum; (b) aluminum-gold-aluminum; (c) carbon-aluminum-gold. All material layers facing photon source are of equilibrium thickness (Ref.21).

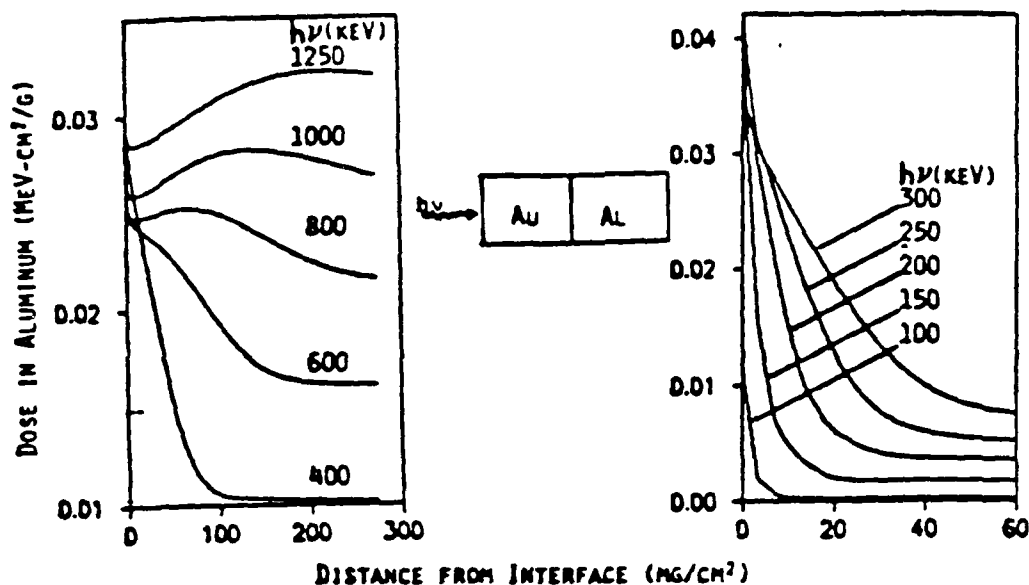


Figure 24. Dose in aluminum next to gold, as calculated by ONETRAN¹, resulting from photons incident on the gold side, for 10 photon energies (Ref.21).

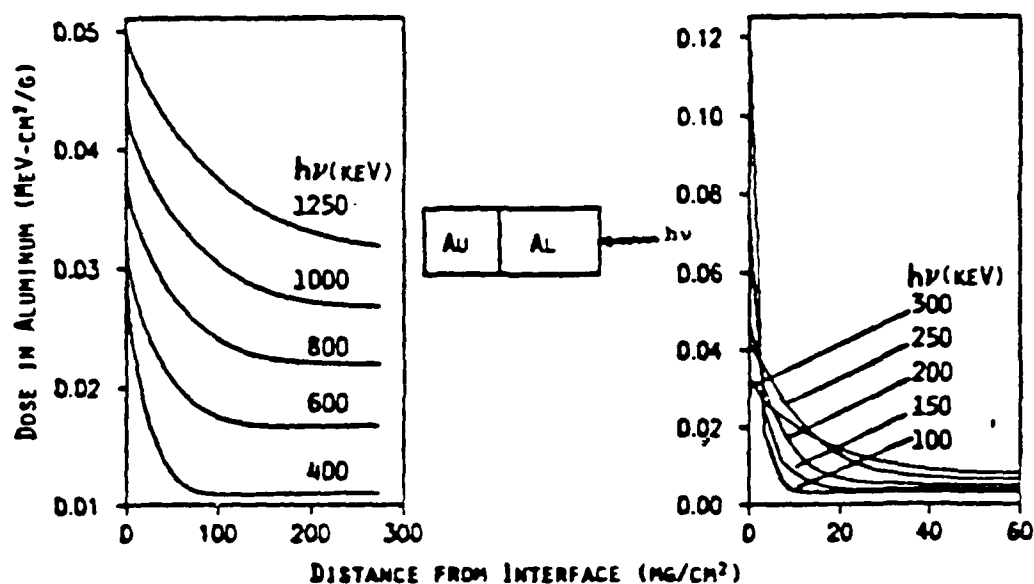


Figure 25. Dose in aluminum next to gold, as calculated by ONETRAN¹, resulting from photons incident on the aluminum side, for 10 photon energies (Ref.21).

points x_m for forward directed (Fig.24) photons, and M dose measurements $B(x_m)$ are taken at points x_m for the back direction (Fig.25). The a_j are the J(unknown) coefficients of the photon spectrum components to be solved for, and the $D_1(x_m, h\nu_j)$, $D_2(x_m, h\nu_j)$ are, respectively, the left-to-right and right-to-left ONETRAN dose profiles corresponding to incident photon energy $h\nu_j$.

Fig.26 shows the best four component spectrum fit to the Au/Al case (Fig.23a), 74.03% 1250 keV, 5.73% 300 keV, 12.44% 200 keV and 8.54% 150 keV. A three component spectrum and a two component spectrum were also found to fit the experimental data fairly well. However, as would be expected, the four component spectrum resulted in the smallest rms deviation of the fit to the data. The full results for this and other cases, component coefficients and rms deviations, are given in Table 2. Fig.27 shows the four component spectrum fit to the experimental data for the Al/Au/Al case (Fig.23b) with the 25.4 μ m gold layer. While the resulting spectrum coefficients are slightly different for this case than those found for the Au/Al configuration, it was found that application of the photon spectrum obtained for the Au/Al case to Al/Au/Al also resulted in a good, although sub-optimal, fit to the data (see Fig.28). Application of this four component spectrum to the C/Al/Au configuration resulted, for reasons as yet unexplainable, in a good fit for the forward directed photon source, but a poor fit for the back-directed photons.

It was found that when all of the Wall and Burke²² data considered were used in the least-squares fitting procedure, the best overall representation of this data was achieved with the following four component spectrum, 73.4% 1250 keV, 9.4% 300 keV, 8.0% 200 keV and 9.2% 150 keV. In a recently performed ion-chamber experiment in which Cobalt-60 source spectrum measurements were made²⁴, the results were found to be consistent with our theoretical findings. Furthermore, the photon spectrum reported here is also consistent with POEM²³ code and MCNP^{25,26} Monte Carlo simulations of Cobalt-60 photon scatter.

Table 2 presents the complete set of two, three, four and five component photon spectra calculated by means of least-squares fits to the Wall and Burke²² experimental data. As can be seen, some of the five component spectra are unsuitable, as evidenced by the negative coefficients. However, when most of the experimental data is used (as shown in columns 3,4,5 of Table 2), the magnitude of the negative component is small. This is an indication that the 250 keV component does not really contribute. This conclusion was reinforced by the application of the t-distribution test, a statistical method for determining confidence levels for the calculated spectrum coefficients.

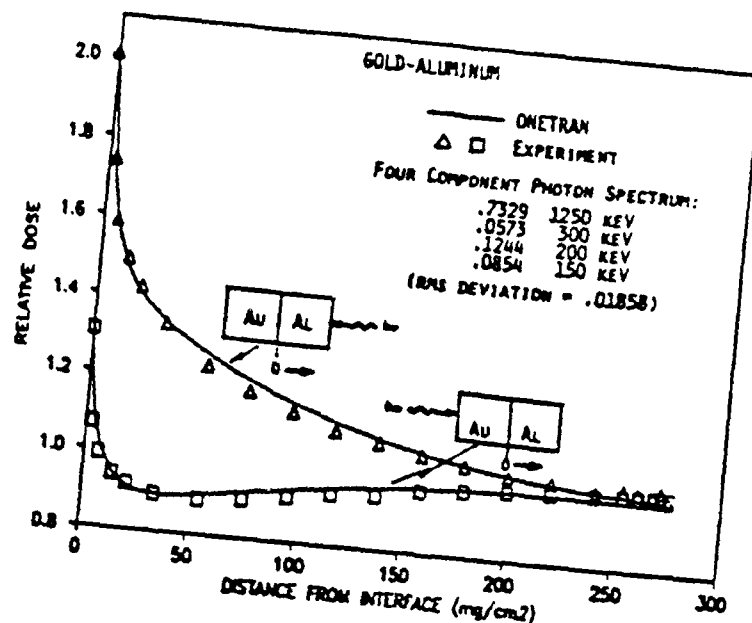


Figure 26. Relative dose vs. distance in aluminum next to gold as calculated with ONETRAN¹ for a four component photon spectrum and measured with a multi-layer aluminum ionization chamber^{2,2} (Ref.21).

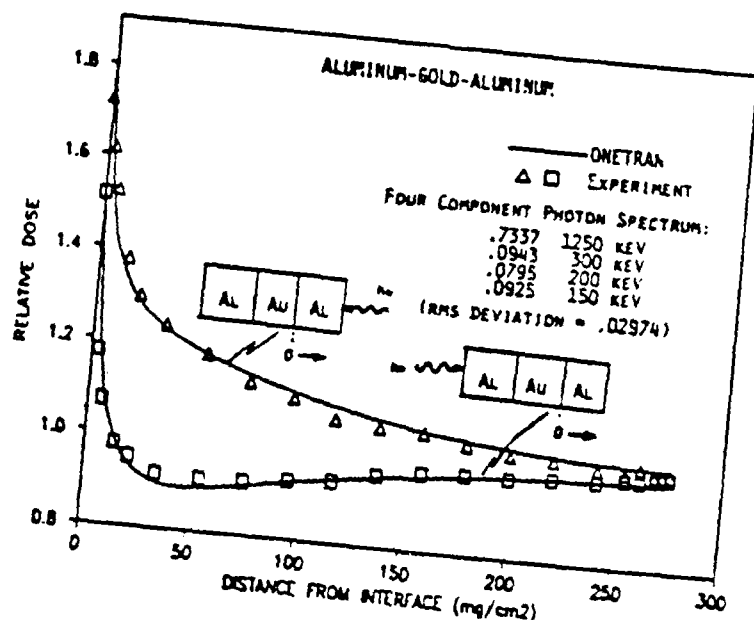


Figure 27. Relative dose vs. distance in aluminum for the three layer Al/Au/Al geometry, as calculated with ONETRAN¹ for a four component photon spectrum and measured with a multi-layer aluminum ionization chamber^{2,2}. Thickness of Au layer = 25.4 μm (Ref.21).

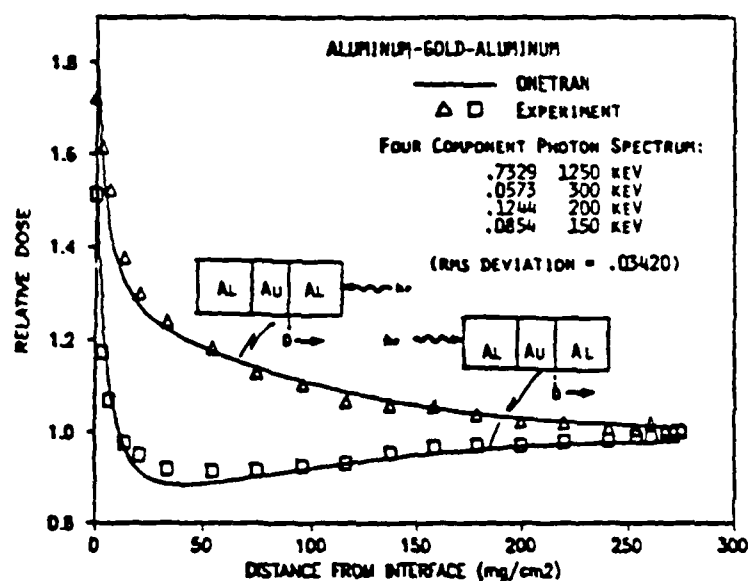


Figure 28. Relative dose vs. distance in aluminum for the three layer Al/Au/Al geometry, as calculated with ONETRAN¹ for a four component photon spectrum and measured with a multi-layer aluminum ionization chamber²². The four component photon spectrum is the same as calculated for the two layer Au/Al geometry (see Fig.26). Thickness of Au layer = 25.4 μ m (Ref.21).

Table 2.

Calculated Photon Spectra (Ref.21)

Photon Energies (keV)	Au/Al ¹	Au/Al ¹ , Al/Au/Al ¹ 25.4 μ m Au ¹ , 12.7 μ m Au ²	Au/Al ¹ , Al/Au/Al ¹ 25.4 μ m Au ¹ , 12.7 μ m Au ² , 6.35 μ m Au ³	Al/Au/Al ¹ 25.4 μ m Au ¹ , 12.7 μ m Au ² , 6.35 μ m Au ³	Al/Au/Al ¹ 12.7 μ m Au ¹ , 6.35 μ m Au ²	Al/Au/Al ¹ 6.35 μ m Au ¹
1250	.7403	.7525	.7519	.7547	.7515	.7557
200	.2597	.2475	.2481	.2453	.2485	.2443
rms deviation	.02267 ¹	.02352 ¹ .02922 ²	.02337 ¹ .02946 ² .03583 ³	.02375 ¹ .02919 ² .03593 ³ .03421 ⁴	.03605 ¹ .03402 ²	.03372 ¹
1250	.7408	.8071	.7956	.8000	.7662	.7794
250	.1453	.0588	.0498	.0473	.1046	.0943
150	.1139	.1341	.1546	.1522	.1293	.1263
rms deviation	.01864 ¹	.03630 ¹ .03409 ²	.03272 ¹ .04085 ² .03953 ³	.03214 ¹ .04200 ² .03903 ³ .02956 ⁴	.03223 ¹ .02861 ²	.02705 ¹
1250	.7329	.7363	.7318	.7337	.7247	.7167
300	.0573	.0897	.1008	.0943	.1193	.1331
200	.1244	.1042	.0792	.0795	.0378	.0331
150	.0854	.0698	.0882	.0925	.1182	.1171
rms deviation	.01858 ¹	.02123 ¹ .02775 ²	.02025 ¹ .02906 ² .03047 ³	.02037 ¹ .02974 ² .03026 ³ .02861 ⁴	.02999 ¹ .02754 ²	.02687 ¹
1250	.7365	.7367	.7297	.7312	.7260	.6516
300	.0291	.0892	.1055	.0998	.1091	.2725
250	.0613	.0007	-.0041	-.0048	.0350	-.1398
200	.0796	.1035	.0806	.0815	.0028	.1276
150	.0935	.0699	.0883	.0923	.1271	.0881
rms deviation	.01853 ¹	.02153 ¹ .02811 ²	.02061 ¹ .02942 ² .03074 ³	.02085 ¹ .02990 ² .03064 ³ .02896 ⁴	.03016 ¹ .02757 ²	.02677 ¹

II.6 Input Processor Programs for ONETRAN Electron Transport Calculations

II.6.1 Program FRONT

The ONETRAN discrete ordinates code was originally written to solve neutron transport problems. Because of this it contains many input options and code features that are useful for research in the nuclear reactor field but not necessarily useful for electron transport calculations in solids, typically of small ($<100\text{ }\mu\text{m}$) dimension, which have been exposed to external radiation sources such as electron beams, gamma or x-rays. For this reason we have not only made major modifications to ONETRAN which have reduced the code to approximately one-half of its original size, but also have written a front-end input processing program, FRONT, which greatly simplifies the process of entering input data into ONETRAN.

Program FRONT generates input data for ONETRAN for both electron beam and photon sources. The program produces a formatted data file configured to be compatible with the ONETRAN input format. This file contains the information necessary to specify the problem geometry and source type. It also contains the ONETRAN-compatible multigroup cross section table for electrons. The code requires only a small amount of "manually" generated user input. Electron scattering cross section and stopping power data are supplied to it by a separate program, a shortened version of DATPAC². If the primary radiation source is gamma-or x-rays rather than electron beam, a multigroup electron source consisting of secondary electrons resulting from photon interactions within the target material is generated by another program, ESRCE. FRONT accepts the ESRCE data and converts it into a format compatible with ONETRAN.

As it is presently configured, FRONT will operate for a maximum of 40 energy groups, 6 coarse spatial mesh zones, 2 materials and a maximum anisotropy in scattering kernel and flux calculations of 12 (i.e. an S_{12} calculation). These limitations are not irrevocable but represent a tradeoff combination of parameter values which will yield a reasonably sized ONETRAN calculation. For practical purposes, the size restriction can be eliminated by running ONETRAN on a virtual memory system such as exists on VAX computers. Work has already begun in this direction. Using a minicomputer system such as VAX facilitates experimentation with problem parameters such as spatial mesh size and number of energy groups.

Presently, electron energy groups of constant width ΔE_g are assumed in FRONT, even though this restriction is not required by the ONETRAN calculation. The group width enters the ONETRAN

calculation through the downscatter cross section, $\sigma_{g, g+1}$ (see Eq.6, section II.2.1.2).

II.6.2 Program ESRCE for Calculating Compton and Photo-electron Energy-Angle Source Distributions

For electron sources which consist of x-ray or gamma-ray produced secondary electrons it is necessary that the Compton and photo-electron energy and angle distributions in the target material(s) be pre-computed and entered as input to ONETRAN. Our program, ESRCE, calculates the multigroup electron source for such a problem. The basic algorithms are adapted from the POEM code²³. In the case of Compton scatter, the program produces a table of the energy-angle distribution of the recoil electrons in accordance with the Klein-Nishina differential cross section and the one-to-one relationship between the recoil angle and the electron kinetic energy²⁶. While the recoil angle is uniquely determined for a given recoil energy, the ONETRAN code requires that the electron source angular distribution be expressed in terms of a series expansion, such as a Legendre series. Since it is not possible to adequately represent a delta function in angle with a finite, reasonably small, Legendre series, ESRCE approximates the angular distribution with a finite Legendre series that peaks at the recoil angle. For this purpose, we have chosen to borrow the functional form of the screened-Rutherford formula, since it is possible to conveniently evaluate the Legendre coefficients for this distribution by means of a simple recursion relation²⁷. The program automatically selects the lowest value of the screening parameter which yields a positive angular distribution for all angles. In this way the sharpest peaking, for this functional form at least, at the value of the recoil angle is guaranteed, consistent with a positive angular distribution.

In addition to the Compton electron distribution, ESRCE also calculates the photo-electron energy-angle distributions for whatever photoelectric interactions that may be of significance, K-photo, L-photo and Auger. Since these angular distributions are not sharply peaked, calculation of their Legendre coefficients is done by means of straightforward numerical integration.

The code contains switches, in the form of input parameters, which allow the user to suppress any of the four components of the secondary electron source. In this way we are able to isolate one or more of these components and make a high resolution (40 or more energy groups) ONETRAN calculation for each source component. The results of these runs, when combined, can then be compared with that obtained when all source components are run in ONETRAN together. This is a useful practice for assessing the accuracy and validity of the secondary electron source specification in a discrete ordinates

calculation. There are checks that can be employed on the results of such calculations. For instance, equilibrium dose calculations can be made both analytically (by hand) and numerically (ONETRAN). These calculations can be made separately for each electron source component. This procedure was useful in "tuning" the secondary electron source algorithms.

III. MONTE CARLO CODE (MCSS) FOR THE ANALYSIS OF ELECTRON TRANSPORT IN INSULATING STRUCTURES AND ASSOCIATED STATISTICAL ANALYSIS COMPUTER CODES

III.1. Introduction

An electron Monte Carlo code, MCSS (acronym for Monte Carlo Single Scatter), was developed to analyze electron trajectories in insulators. It has been and continues to be used as a research tool at RADC/ESR. Preliminary testing has been done for electron transport in SiO_2 . The results thus far obtained, some of which are reported in Ref.28, indicate that the transport calculations yield physically reasonable answers. In its current form it is used to analyze the situation where electron beam sources with energies ranging from 600 keV down to perhaps 1 keV, are incident on thin (ranging from 1 down to .02 μm) insulating films such as SiO_2 .

III.2 Electron Transport Model

In the design of the Monte Carlo code an effort was made to base its operation on a straightforward electron transport model, a collision-by-collision trace of each electron track, using interaction probabilities based on realistically treated scattering processes. It may be argued that such collision-by-collision calculations are nearly impossible to perform in a realistic situation. However if the insulating film is sufficiently thin, such calculations as this are feasible since high energy electrons escape readily before undergoing many scatters. The only remaining problem is then that of tracing lower energy secondary electron trajectories as they course through the scattering material.

A beam of electrons is assumed incident on the insulator target. There is a probability that some of the incident electrons will undergo collisions with other electrons and nuclei in the target, while others will pass uncollided through the target. The probability of the electron undergoing an interaction is, as is well known, proportional to the total scattering cross section. In our Monte Carlo calculation, the primary electron penetration distance, Δs , to the point of first collision in the target is calculated as

$$\Delta s = -\lambda(E)\log\xi, \quad (15)$$

where $\lambda(E)$ is the total mean free path of the electron with energy E , and ξ is a (pseudo) random number selected from the uniform distribution (0,1). The total mean free path, or rather, the total cross section, $\sigma(E)$, can be calculated from one or more formulas, or taken from a table of $\sigma(E)$ vs. E . The MCSS Monte Carlo code makes use of a highly detailed cross section set

supplied by the Oak Ridge National Laboratory Health and Safety Research Division²⁹. A description of these cross sections will be given in a later section.

After the first collision of the electron, with either another electron or a nucleus, the post-collision primary electron energy and scattering angle are determined. The primary electron is transported to the point of next collision in accordance with Eq.15 to determine the distance between collisions, Δs . The above procedure is repeated until the primary electron either escapes from the medium or its energy falls below a designated cut-off value. It was found that when this program was run for the case of a 600 keV source beam, with 1000 trajectory case histories, all of the 600 keV primaries escape from the 1 μm thick SiO_2 medium via transmission. Some scatters did occur however, and gave rise to secondary electron production.

If an inelastic electron-electron scattering event occurs, and if ionization rather than excitation results, the coordinates of the collision site (or hole site) are recorded. The position, energy and direction cosines of the secondary electron produced by the ionizing collision are recorded, and the secondary electron is put into an electron "bank". After all of the primary electron case histories have been run, the entire Monte Carlo process is repeated (i.e. the program is re-run) but with the contents of the secondary electron bank (or buffer) serving as the new primary electron source. In each Monte Carlo run, each primary electron case history is run until either the electron has escaped from the medium or its energy has fallen below the threshold for inelastic scatter (8.89 eV) for SiO_2 . The Monte Carlo program is re-run a sufficient number of times until all higher generation electrons have either fallen below the threshold or have escaped. Throughout the computations the coordinates of hole sites and final electron positions (where an electron has lost all of its energy) are recorded on files for subsequent analysis. A more detailed description of our Monte Carlo electron transport program follows.

III.3. Program Description

III.3.1 MCSS (=Main Program)

This program calls the various subroutines necessary for the electron transport calculation. Every case history is initiated by the main program, and after the appropriate number of case histories is run, the main program halts the calculation.

III.3.2 SETRUN

The primary function of this subroutine is the initialization of the various parameters necessary to perform the Monte Carlo calculation. Among the parameters specified are those

describing the physical properties of the primary electron source, such as source energy (MeV), incident beam obliquity and coordinates of the point where the primary beam strikes the target. Also specified are the physical properties of the target material such as density, thickness and ionization cut-off energy. Additional parameters required for the calculation are initialized here such as the number of primary electron case histories to be run and a source option switch to indicate whether the source electrons originate from an external electron beam (used in the first iteration) or from the secondary electron bank. A printout is made of the initialized parameters.

This subroutine also calls subroutine ESET to process the energy dependent cross section and angular scattering information.

III.3.3 ESET

The purpose of this subroutine is to incorporate the cross section and angular scattering distribution tables into the calculation. Presently, these tables, which are supplied by ORNL²⁹ are of four basic types: 1)inelastic scattering cross section; 2)elastic scattering differential(energy) cross sections for silicon and oxygen; 3)elastic scattering double differential (energy and angle) cross sections for silicon and oxygen; 4)elastic scattering total cross sections. The inelastic cross sections are separated into five components according to whether the inelastic scatter occurs with a valence electron, an oxygen K-shell electron, silicon 2p shell, silicon 2s shell, or silicon 1s shell. The exact manner in which these cross sections are utilized to determine event probabilities, energy losses and angular scattering directions is discussed in the ENERGY subroutine description.

III.3.4 SETHIS

Each time an electron case history is begun, this subroutine is called to initialize the electron track parameters such as the coordinates (x,y,z) of the electron position, polar and azimuthal angles (θ, ϕ) specifying the direction of the electron's motion, electron energy(E), and total interaction mean free path ($\lambda(E)$). When initiating an electron case history, this subroutine distinguishes between a primary source electron and an n-th ($n > 1$) generation electron. An additional parameter, the case history identifier number, is also initialized. This last parameter is required to preserve, from one electron generation to the next, the identity of all of the secondary, tertiary, etc. electrons resulting from a particular primary electron. Each electron generation is produced by a separate run of MCSS. With this case history identifier, all subsequent electron tracks originating from one primary electron can be gathered together for processing by a statistical analysis program.

III.3.5 PENET

The primary function of this subroutine is that of translating the electron to the point of next collision and calculating the new electron position coordinates. The intercollision distance is computed according to Eq.15. In addition, PENET also performs the function of checking to determine if the electron case history should be terminated. This condition can occur in either of two ways: 1) the electron can exit from the scattering medium (transmission or reflection); or 2) the electron energy can fall below the ionization threshold (8.89 eV for SiO₂, although in practice a threshold of 10 eV is used since the cross section table ends there). When this latter condition occurs, as it inevitably does for most of the higher($n > 1$) generation electrons, subroutine LOWEND is called to determine the final position of the electron.

III.3.6 ENERGY

When a collision has taken place, the first task of subroutine ENERGY is to determine whether an elastic (electron-nuclear) or inelastic (electron-electron) scattering has occurred. A search is made of the total elastic and inelastic cross section tables to determine, via interpolation, the cross section values appropriate to the electron energy, E . The probability, P_e , of an elastic scatter is given by

$$P_e = \frac{\sigma_e(E)}{\sigma_e(E) + \sigma_i(E)} \quad (16)$$

where $\sigma_e(E)$ and $\sigma_i(E)$ are, respectively, elastic and inelastic scatter cross sections for an electron of energy E . A random number, ξ , uniformly distributed on the interval (0,1) is then compared with the elastic scattering probability, P_e . If $\xi < P_e$, the scattering is assumed elastic. Conversely, if $\xi > P_e$, the scattering is taken to be inelastic.

For the first of these situations, elastic scattering, the remaining task of subroutine ENERGY is the calculation of the angular deflection of the electron as a result of having undergone an electron-nuclear scatter. Since the target nuclei masses, M , are so much greater than the electron rest mass, m (e.g. $M/m \approx 50000$ for silicon), it is assumed that the energy lost by the electron is negligibly small. The energy of the elastically scattered electron is taken to be the same after collision as before.

Calculation of the angular deflection for elastically scattered electrons is done as follows: if the electron energy, E , is above 300 keV, it is assumed that no angular deflection occurs. The angular scattering cross sections are so forwardly peaked in the neighborhood of 300 keV that no values are listed for energies above 300 keV. The cross section compilation³⁵

incorporates the assumption of zero angular deflection above 300 keV. Below 300 keV however, the angular deflection of the electron can be calculated. If the scattering material is a chemical compound, such as SiO_2 , it is necessary to determine which of the nuclei, silicon or oxygen, the electron has collided with. In our code, energy interpolations of the total elastic cross section tables for silicon and oxygen are made. The collision probability for a silicon nucleus, $P_{e,si}$, is calculated as

$$P_{e,si} = \frac{\sigma_{e,si}(E)}{\sigma_{e,si}(E) + \sigma_{e,o}(E)} \quad (17)$$

where $\sigma_{e,si}(E)$ and $\sigma_{e,o}(E)$ are the elastic scatter cross sections for an electron of energy E with silicon and oxygen nuclei, respectively. A random number, ξ , uniformly distributed on the interval $(0,1)$ is then compared with $P_{e,si}$. If $\xi < P_{e,si}$ the elastic scatter is assumed to have occurred with a silicon nucleus; otherwise if $\xi > P_{e,si}$, scatter with oxygen is assumed. To determine the angular deflection resulting from the elastic scatter, another random number game is played on the cumulative integral $\sigma(E, \omega)$, of the double differential (energy, angle) cross section, where ω is the scattering angle. This cross section table is given in the form of a cumulative probability for scatter through angle ω , so that when a random number uniform on the interval $(0,1)$ is selected, it is compared with the angular deflection probability table, and ω is thus obtained directly.

Inelastic electron-electron scatter is treated differently from the above. When such an event is determined to have occurred, it must be determined whether the collision occurred with a valence, oxygen K-shell or silicon 1s, 2s or 2p shell electron. This is accomplished by calculating the cumulative probability that each of these five events will occur, given an incident electron of energy E . Since the individual cross sections for the five units are listed as a function of energy, this process is straightforward. These five cross sections are listed in the following order: σ_{val} , σ_{o-k} , σ_{si-2p} , σ_{si-2s} , σ_{si-1s} (the energy dependence is suppressed here for brevity). The sum of these five cross sections is $\sigma_i(E)$ as defined in Eq.16. The cumulative probability for, say, inelastic scatter with a silicon 2p electron is then

$$P_{si-2p} = \frac{\sigma_{val} + \sigma_{o-k} + \sigma_{si-2p}}{\sigma_i(E)} \quad (18)$$

To decide which of these five possible inelastic scattering events have occurred, another random number, ξ , is drawn and compared with each of the five cumulative probabilities. (The fact that all five inelastic scattering events are not always energetically possible is automatically accounted for by zero

cross section values in the table.) If for example

$$P_{Si-2p} < \xi \leq P_{Si-2s} , \quad [19]$$

the event is assumed to be an inelastic scatter with a silicon 2s electron. Once this event selection has been made, the remaining tasks are: 1) calculate the energy lost by the incident electron; 2) calculate the energy of the secondary electron; 3) calculate the angular deflection of the primary electron.

To determine the energy loss, w , of the primary electron, the first of the above four tasks, a table is consulted of cumulative probabilities, $P(w)$ versus the fractional energy loss, $f(w)$, for the incident electron for each of the five inelastic scatter categories. For an energy loss w , the cumulative probability, $P(w)$, of occurrence is given as

$$P(w) = \frac{\int_{w_1}^w \frac{d\sigma}{dw}(E, w) dw}{\int_{w_1}^{w_2} \frac{d\sigma}{dw}(E, w) dw} , \quad [20]$$

and the fractional energy loss, $f(w)$, is given as

$$f(w) = \frac{w - w_1}{w_2 - w_1} , \quad [21]$$

where w_1 is the ionization threshold energy for the inelastic scatter process under consideration (i.e. 8.89 eV for valence electrons, 108.17 eV for Si-2p) and w_2 is the corresponding maximum possible energy loss for the incident electron of energy E . A random number, ξ , is compared with the $P(w)$ table, the corresponding value of $f(w)$ is obtained, and finally the energy loss value w (by inversion of Eq.21).

The energy of the secondary electron, E_{sec} , is calculated as the energy lost by the primary electron minus the threshold energy. That is

$$E_{sec} = w - w_1 , \quad [22]$$

A call to subroutine SCORE (to be described later) is made to record the coordinates of the ionization (or hole) site and to "deposit" the secondary electron in the "bank". The post collision energy E' , of the primary electron is calculated as

$$E' = E - w . \quad [23]$$

Finally, the angular deflection, θ , of the primary electron following an inelastic collision is calculated as³⁰

$$\sin^2 \omega = \frac{E_{\text{sec}}/E}{1+E/1.02195} \quad [24]$$

where all energies are expressed in MeV.

III.3.7 ANGLES

After the coordinates of a collision site have been computed by PENET, and the new electron energy and mean free path have been computed by ENERGY, the change in direction of motion (in the inertial frame) is determined. Given the scattering angle ω as computed by subroutine ENERGY, the post-collision polar angle functions $\cos\theta$ and $\sin\theta$ and azimuthal functions $\cos\phi$ and $\sin\phi$ are computed from the pre-collision values by means of standard spherical trigonometric relations.

III.3.8 LOWEND

When the electron energy E falls below the ionization cut-off energy (8.89 eV), subroutine LOWEND is called to terminate the case history. A procedure has been developed to accomplish this task which makes use of cross section and stopping power information supplied by Ritchie, Hamm et al.²⁹ The elastic scattering cross section for SiO_2 is approximately 450 times greater than the inelastic cross section for 10 eV electrons. Since no further ionizations can result from inelastic scatters at this energy, no additional electron-hole pairs will be created. The only remaining information to be gathered pertaining to the electron is its position when it has surrendered all of its energy. At present the approximation is made that elastic scattering of electrons below 10 eV is characterized as isotropic in angle.

Also at present, the energy loss mechanism in this low energy range is approximately represented by a fairly simple stopping power function²⁹. In the energy range 10 eV down to 1 eV, this stopping power function can be closely approximated by a straight line on a log-log plot which then translates into the approximate expression

$$\frac{dE}{dx} \approx \frac{-3.32}{E} \quad [25]$$

where dE/dx is now given in units of MeV-cm²/g and E is expressed in eV. It may be noted that the inelastic energy loss mechanism in the energy range of interest here is phonon excitation rather than excitation via electron-electron scatter.

This subroutine makes use of the stopping power formula (Eq.25) to terminate the electron case history in the following way. A penetration distance Δs is calculated in the same manner as in Eq.15, namely

$$\Delta s = -\lambda_e(10\text{eV})\log\xi, \quad (26)$$

where, as before, ξ is a random number and $\lambda_e(10\text{eV})$ is the elastic scattering mean free path. Then since the electron is assumed to have traveled a path length increment Δs , the corresponding energy decrement is taken as

$$\Delta E = -\left|\frac{dE}{dx}\right|\Delta s. \quad (27)$$

A set of direction cosines is chosen from a uniform random sampling of an isotropic angular distribution, and the electron is then translated another Δs increment along the new direction. This procedure is repeated until the electron energy falls below 1 eV, at which point its final position is recorded. (Provision is also made for history termination via escape from the medium).

The algorithm for terminating electron histories in the low energy range that has been described above is a temporary one. It is anticipated that a more physically detailed model for the scattering of electrons in the energy range below 10 eV will be incorporated in future versions of MCSS.

III.3.9 SCORE

When an electron undergoes an inelastic collision resulting in an ionization, the coordinates of the collision point (hole site), scattering deflection angle, energy loss, secondary electron energy and case history label are entered into a buffer array for processing by subroutine NEXTGEN. Subroutine SCORE is also called when an electron history is terminated either as a result of an electron "death" (loss of all of its energy) or an escape from the medium. When a case history is terminated, the pertinent information(position, energy, history label) is recorded in the buffer array.

III.3.10 NEXTGEN

The function of this subroutine is to gather all of the information recorded by subroutine SCORE (hole site, secondary electron data and history termination data) from all iterations of MCSS and systematically place it all in a data bank for later analysis. It also reformats the secondary electron data from any one given generation so that it may be used as the electron source for the next generation.

III.4 Statistical Analysis Computer Codes for the Analysis of Charge Distributions in Insulators as Calculated by the MCSS Monte Carlo Code

III.4.1. Introduction

As reported in the previous sections of this chapter, the Monte Carlo code MCSS calculates and stores such data as the positions of hole creations (ionization sites) and the coordinates of electrons which have lost practically all of their energy through a succession of collisions. This information constitutes, in general, voluminous data files, for which it became necessary to develop statistical analysis programs to sort through these files to view the results of the Monte Carlo calculation in a compact and coherent form. Two codes were written to perform the statistical analysis of the Monte Carlo data. One code analyzes the data for proximity and nearest neighbor distributions, while the second code identifies and analyzes electron and hole clusters. The results obtained with the proximity analysis and cluster analysis programs can be useful in determining electron-hole recombination probabilities. A brief description of these analysis programs follows.

III.4.2 Generation and Analysis of Proximity Statistics for Electron-Hole and Hole-Hole Pairs

The first of the two analysis codes (DISTRIB) produces four tables of statistics for each primary electron case history generated by MCSS. The first is a tabulation of the proximity function for hole-electron pairs and hole-hole pairs. The program sorts through the output data file of MCSS and, for a particular case history, selects out all of the hole and electron position data. (The code is currently set up to handle as many as 100 case history analyses per run.) All of the hole sites for a particular history are then sorted in increasing order of depth in the insulating material. A tally is made of the distance between every pair of holes and every electron-hole pair. Then a set of 15 spherical shell boundaries with radii ranging from 5 to 500 Angstroms is "drawn" about every hole site, and a table is made of the cumulative number of electrons inside each of these imaginary spheres centered at the hole site. Figure 29 is an example of such a table. As shown for case history number 580 (which will be used for illustrative purposes through this section), there are 16 hole sites and 16 electron "death" (energy less than 1 eV) sites. The table shows the z-coordinate (Fig.29) in Angstroms (second row across the top) of each of the 16 hole sites. A vertical listing is made of the number of electrons (E's) and holes (H's) within the 15 spheres.

The second table (see Fig.30a) is a set of mean values, averaged over all hole sites (16 in this instance), of the number of electrons and holes inside the 15 spherical boundaries.

ANALYSIS OF HISTORY NO. 580
TOTAL ENERGY LOSS (MEV) = .30810E-03

NO. OF 600 LINE RECORDS = 1
RECORD NO. 1
NO. OF ELECTRONS = 16
NO. OF HOLE SITES = 16

HOLE SITE	1	2	3	4	5	6	7	8	9	10
Z VALUE (ANG)	1160.8	1873.8	1883.5	8128.2	8250.7	8368.5	8368.1	8371.8	8372.2	8372.3
SPHERE RAD(ANG)	E'S H'S	E'S H'S	E'S H'S	E'S H'S	E'S H'S	E'S H'S	E'S H'S	E'S H'S	E'S H'S	E'S H'S
5.0	0	0	0	0	0	0	0	0	0	0
10.0	1	0	0	0	1	0	0	1	1	1
20.0	2	0	0	0	1	0	0	2	2	2
30.0	2	1	1	0	2	2	1	4	4	4
50.0	2	1	2	0	1	3	3	6	6	5
75.0	2	1	1	0	2	3	4	5	5	5
100.0	2	1	2	0	2	5	6	5	5	5
125.0	2	1	1	1	3	7	7	7	7	7
150.0	2	1	1	2	6	8	8	8	8	8
175.0	2	1	2	2	6	8	8	8	8	8
200.0	2	1	1	2	8	8	8	8	8	8
250.0	2	1	2	6	8	8	8	8	8	8
300.0	2	1	1	8	8	8	8	8	8	8
400.0	2	1	2	8	8	8	8	8	8	8
500.0	2	1	2	8	8	8	8	8	8	8

HOLE SITE	11	12	13	14	15	16	17	18	19	20
Z VALUE (ANG)	6474.5	8855.3	8710.1	8737.3	8814.1	8905.1	8905.1	8905.1	8905.1	8905.1
SPHERE RAD(ANG)	E'S H'S	E'S H'S	E'S H'S	E'S H'S	E'S H'S	E'S H'S	E'S H'S	E'S H'S	E'S H'S	E'S H'S
5.0	0	0	0	0	0	0	0	0	0	0
10.0	1	0	0	0	0	0	0	0	0	0
20.0	1	0	0	0	0	0	0	0	0	0
30.0	2	0	0	0	0	0	0	0	0	0
50.0	2	1	1	2	2	2	2	2	2	2
75.0	2	1	2	2	2	2	2	2	2	2
100.0	2	1	2	2	2	2	2	2	2	2
125.0	4	1	2	2	3	2	2	2	2	2
150.0	5	1	2	2	4	2	2	2	2	2
175.0	6	1	2	2	4	2	2	2	2	2
200.0	8	1	3	2	4	2	2	2	2	2
250.0	8	1	4	2	4	2	2	2	2	2
300.0	8	1	4	2	4	2	2	2	2	2
400.0	8	3	4	2	4	2	2	2	2	2
500.0	9	5	4	2	4	2	2	2	2	2

Figure 29. Electron-hole and hole-hole distances for one primary electron case history (no.580).

SPHERE RADIUS(ANG)	MEAN VALUES FOR THIS HISTORY	
	ELECTRONS	HOLES
5.0	.8250E+01	.13750E+01
10.0	.43750E+00	.13750E+01
20.0	.67500E+00	.18750E+01
30.0	.15000E+01	.23750E+01
50.0	.18750E+01	.25000E+01
75.0	.21250E+01	.25000E+01
100.0	.26250E+01	.26250E+01
125.0	.37500E+01	.36250E+01
150.0	.42500E+01	.42500E+01
175.0	.44375E+01	.43750E+01
200.0	.46250E+01	.43750E+01
250.0	.51875E+01	.52500E+01
300.0	.51875E+01	.52500E+01
400.0	.54375E+01	.55000E+01
500.0	.58250E+01	.61250E+01

Figure 30a. Mean values of electron-hole and hole-hole distances for one primary electron case history (no.580).

N(R) VS. R (ANGSTROMS)	
1	.10000E+01 .10000E+01
2	.20000E+01 0.
3	.30000E+01 0.
4	.40000E+01 0.
5	.50000E+01 0.
6	.60000E+01 0.
7	.70000E+01 .30000E+01
8	.80000E+01 .10000E+01
9	.90000E+01 .10000E+01
10	.10000E+02 .10000E+01
11	.11000E+02 0.
12	.12000E+02 0.
13	.13000E+02 0.
14	.14000E+02 .10000E+01
15	.15000E+02 0.
16	.16000E+02 0.
17	.17000E+02 .10000E+01
18	.18000E+02 0.
19	.19000E+02 0.
20	.20000E+02 0.
21	.21000E+02 0.
22	.22000E+02 .10000E+01
23	.23000E+02 0.
24	.24000E+02 0.
25	.25000E+02 0.
26	.26000E+02 0.
27	.27000E+02 0.
28	.28000E+02 .30000E+01
29	.29000E+02 0.
30	.30000E+02 0.

ELECTRON SITE Z VALUE (ANG) SPHERE RAD(ANG)					
	1 623.7 E'S	2 2486.1 E'S	3 2513.8 E'S	4 8989.3 E'S	5 9036.1 E'S
5.0	1	1	1	1	1
10.0	1	1	1	1	1
20.0	1	1	1	1	1
30.0	1	1	1	1	1
50.0	1	2	2	1	1
75.0	1	2	2	1	1
100.0	1	2	2	2	2
125.0	1	2	2	2	2
150.0	1	2	2	2	2
175.0	1	2	2	2	2
200.0	1	2	2	2	2
250.0	1	2	2	2	2
300.0	1	2	2	2	2
400.0	1	2	2	2	2
500.0	1	2	2	2	2

Figure 30b. Electron-electron distances for one primary electron case history (no.580).

Figure 30c. Electron-hole nearest neighbor distribution for one primary electron case history (no.580).

The third table (see Fig.30b) provides the same sort of proximity information for electron-electron distances as was given in the first table for hole-hole and hole-electron distances. Here, the electron, rather than hole, sites are listed in increasing z order (across the top). Of course, there is only one vertical listing, the number of electrons (E's) within the 15 spherical boundaries, since a column of electron-hole distances would only provide a repetition of the information already given in the table of Fig.29.

The last table (Fig.30c) in the series is a listing of the electron-hole nearest distance distribution for the case history under examination. Thirty nearest neighbor distances (in this case 1 to 30 Angstroms in 1 Angstrom increments) are listed. For each hole site, the distance to the nearest electron is calculated. Then, the number, N(R), of hole sites with nearest neighbor distance between successive R values are listed alongside R (for example, in the table shown in Fig.30c, there is one pair with nearest neighbor distance between 0 and 1 Angstrom, 3 between 6 and 7 Angstroms, etc.)

This computer program(DISTRIB) has at present a section of code that can be run optionally. This is a summary package which accumulates proximity statistics for any specified number of case histories and plots the results in concise form. As an example, taking the table shown in Fig.29, the program accumulates over all histories of interest the number (or frequency) of occurrences, F(n), where n can be the integer entry in the table either for the number of electrons or the number of holes within a given sphere. After the frequency distribution F(n) has been determined (by summing over all histories of interest), the distribution F*(n) is computed as

$$F^*(n) = \frac{F(n)}{n} \quad [28]$$

The normalized function $\hat{F}^*(n)$ is then computed as

$$\hat{F}^*(n) = \frac{F^*(n)}{\sum_n F^*(n)} \quad [29]$$

The mean and variance of $\hat{F}^*(n)$ are computed and printed out in addition to a table of $\hat{F}^*(n)$ vs. n. This procedure is performed separately for every sphere radius in the hole-electron proximity table and the electron-electron proximity table. The results are then plotted by the program on a log-log graph. Fig.31 is a sample plot which shows $\hat{F}^*(n)$ vs. n for the 200 Angstrom sphere. The H's indicate the hole-hole occurrences in the neighborhood defined by the spherical boundary, while the E's show the same distribution for hole-electron occurrences. These results represent data summed over 97 case histories.

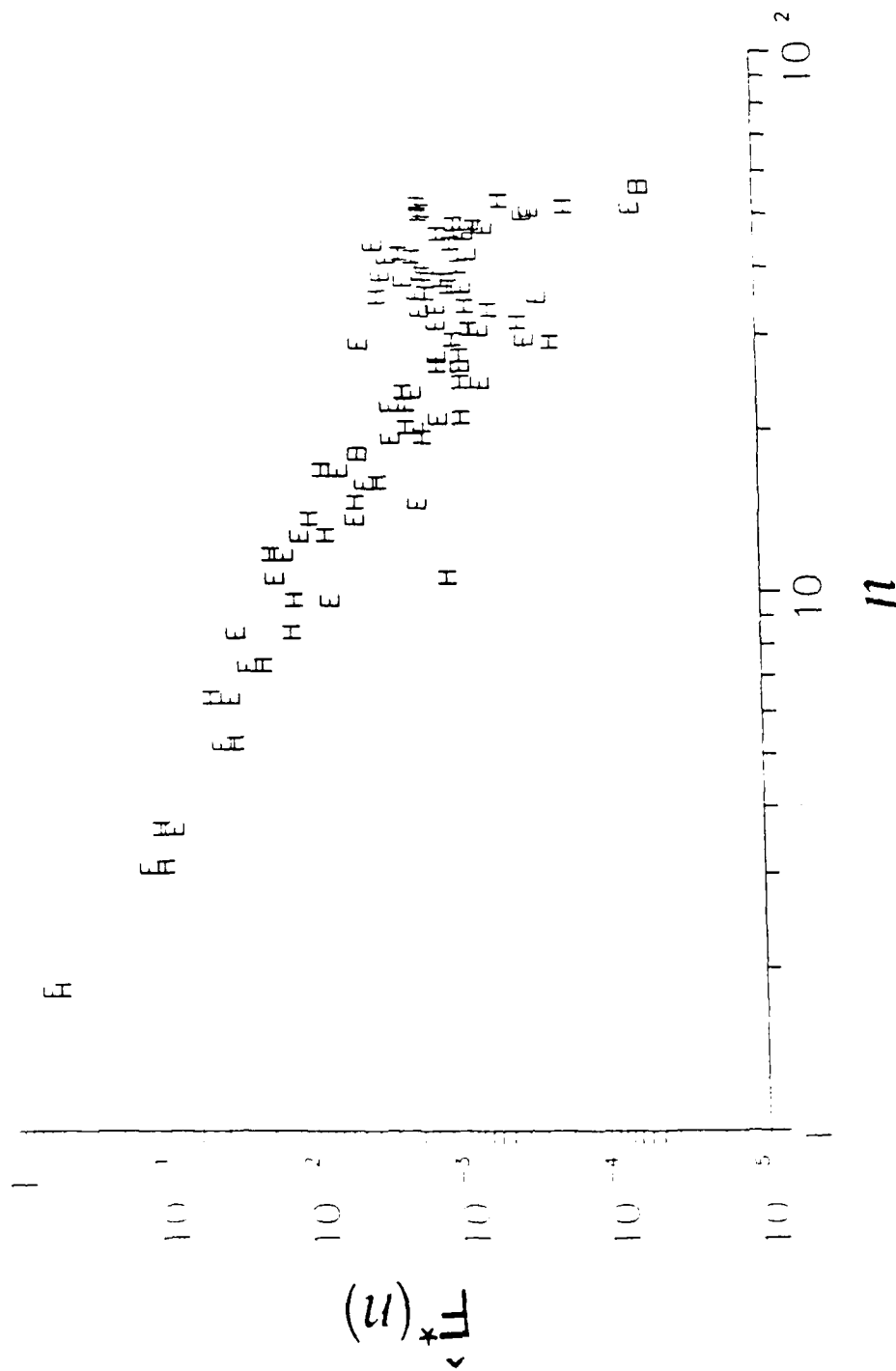


Figure 31. Electron-hole and hole-hole frequency distribution for the 200 angstrom sphere. H's indicate hole-hole occurrences. E's indicate electron-electron occurrences.

III.4.3 Electron and Hole Cluster Analysis Program

The second statistical analysis program to accompany the MCSS Monte Carlo code is a cluster analysis code (CLUSTER). The main function of this program is to identify clusters of electrons or holes as they occur in the insulating material as a result of bombardment by electrons. For a particular primary particle case history, the program identifies all electron sites which are neighbored by another electron within a pre-specified distance. Similarly, neighboring hole sites are also thus identified. A matrix is then formed of all of the electron-electron distances and hole-hole distances for a given case history. Examples of the electron-electron and hole-hole matrices for history number 580 (the same case history used in the example of Fig.29) are shown in Fig.32. All distances are given in Angstroms. The diagonal elements are, of course, zero since these represent the distance between an electron, or hole, and itself. The lower off-diagonal elements are zeroed out since the matrix is symmetric and the information is redundant. A computational mask is then applied to the data which filters out all electron-electron (and hole-hole) cluster occurrences above a specified threshold value. These masks are set at 500, 200, 100, 50 and 20 Angstroms. The "masked" matrices are printed out again in a slightly different format. The non-zero elements above the diagonal are identified with the letter "W", while the lower off-diagonal elements do not appear at all. An example of the application of the five masks to the electron-electron distance matrix is shown in Figs. 33a-e for history number 580.

0	15	739	5087	5112	5175	5201	5201	5221	5307	5313	5717	7568	7575	7744	7750
0	0	733	5082	5106	5169	5195	5196	5215	5301	5307	5712	7562	7570	7738	7744
0	0	0	4356	4381	4442	4470	4470	4489	4575	4581	4986	6837	6844	7013	7019
0	0	0	0	31	121	131	120	140	221	229	632	2483	2490	2658	2664
0	0	0	0	0	116	113	102	119	199	207	606	2457	2465	2633	2639
0	0	0	0	0	0	68	58	71	147	152	554	2397	2403	2573	2579
0	0	0	0	0	0	0	39	36	121	132	521	2368	2375	2545	2551
0	0	0	0	0	0	0	0	22	108	116	519	2368	2375	2544	2550
0	0	0	0	0	0	0	0	0	91	101	500	2349	2356	2525	2531
0	0	0	0	0	0	0	0	0	0	16	414	2263	2270	2439	2445
0	0	0	0	0	0	0	0	0	0	0	410	2258	2264	2433	2439
0	0	0	0	0	0	0	0	0	0	0	0	1852	1859	2028	2033
0	0	0	0	0	0	0	0	0	0	0	0	0	33	182	186
0	0	0	0	0	0	0	0	0	0	0	0	0	0	176	181
0	0	0	0	0	0	0	0	0	0	0	0	0	0	0	12

Figure 32a. Electron-electron distance matrix for history no. 580.

0	717	726	4968	5091	5206	5208	5212	5212	5212	5315	5695	7550	7577	7654	7745
0	0	12	4255	4377	4493	4495	4499	4499	4499	4601	4982	6837	6864	6941	7032
0	0	0	4245	4368	4484	4485	4489	4489	4489	4592	4972	6827	6855	6931	7022
0	0	0	0	129	240	241	244	244	245	349	728	2583	2610	2687	2778
0	0	0	0	0	118	128	128	128	128	227	607	2461	2488	2565	2656
0	0	0	0	0	0	31	23	23	23	116	490	2345	2372	2449	2540
0	0	0	0	0	0	0	15	15	15	121	488	2343	2370	2447	2538
0	0	0	0	0	0	0	0	1	1	112	484	2339	2366	2443	2534
0	0	0	0	0	0	0	0	0	1	111	484	2339	2366	2443	2534
0	0	0	0	0	0	0	0	0	0	111	484	2339	2366	2443	2534
0	0	0	0	0	0	0	0	0	0	0	384	2238	2265	2341	2433
0	0	0	0	0	0	0	0	0	0	0	0	1856	1883	1960	2051
0	0	0	0	0	0	0	0	0	0	0	0	0	30	104	201
0	0	0	0	0	0	0	0	0	0	0	0	0	0	78	172
0	0	0	0	0	0	0	0	0	0	0	0	0	0	0	104

Figure 32b. Hole-hole distance matrix for history no. 580.

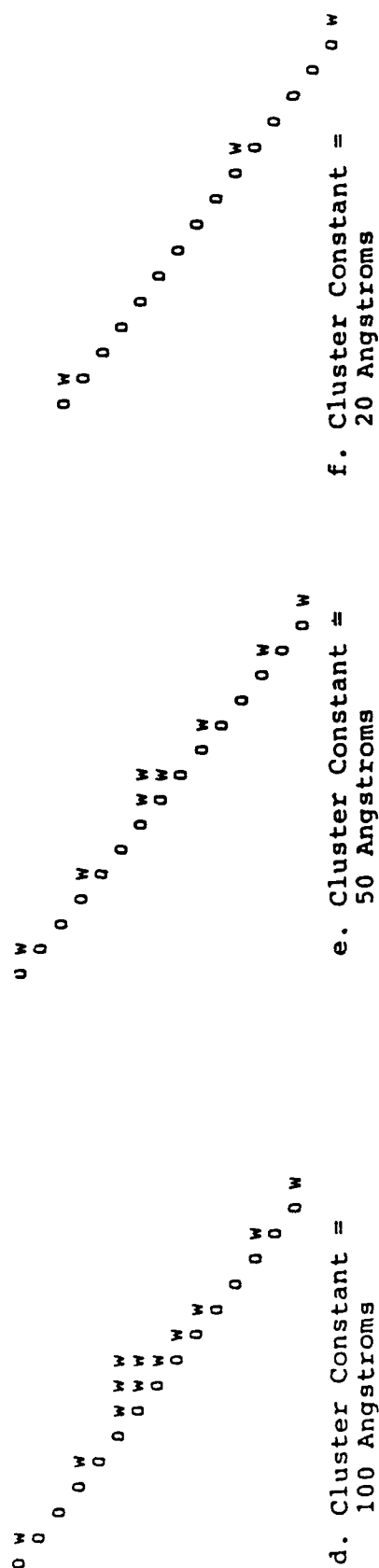
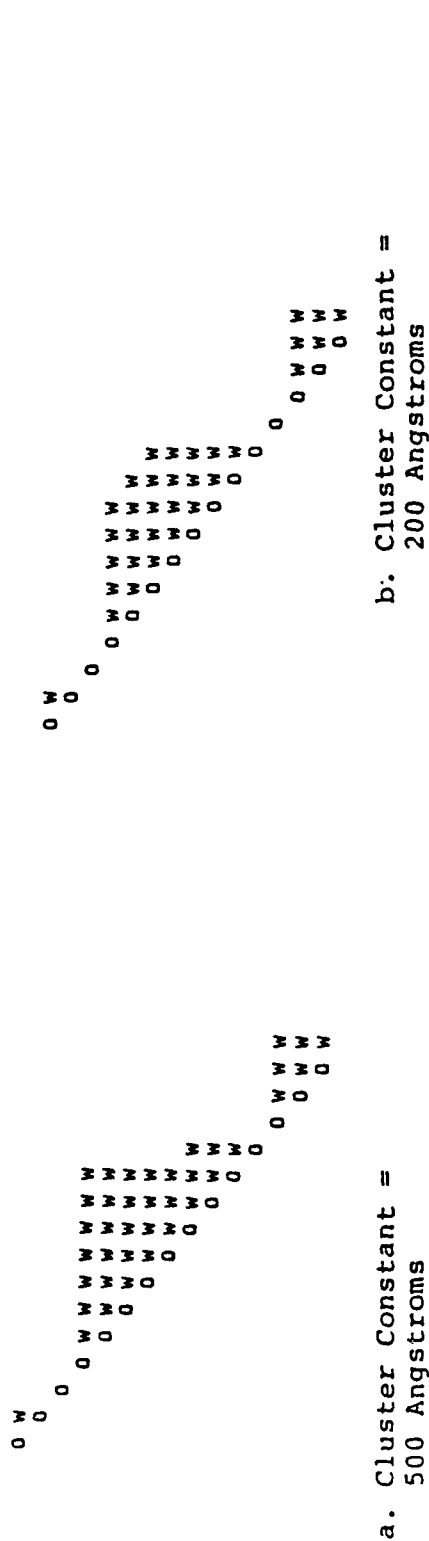


Figure 33. Masked electron-electron cluster matrices.

IV. PHOTON TRANSPORT CALCULATIONS WITH THE MCNP COMPUTER^{3,1} CODE

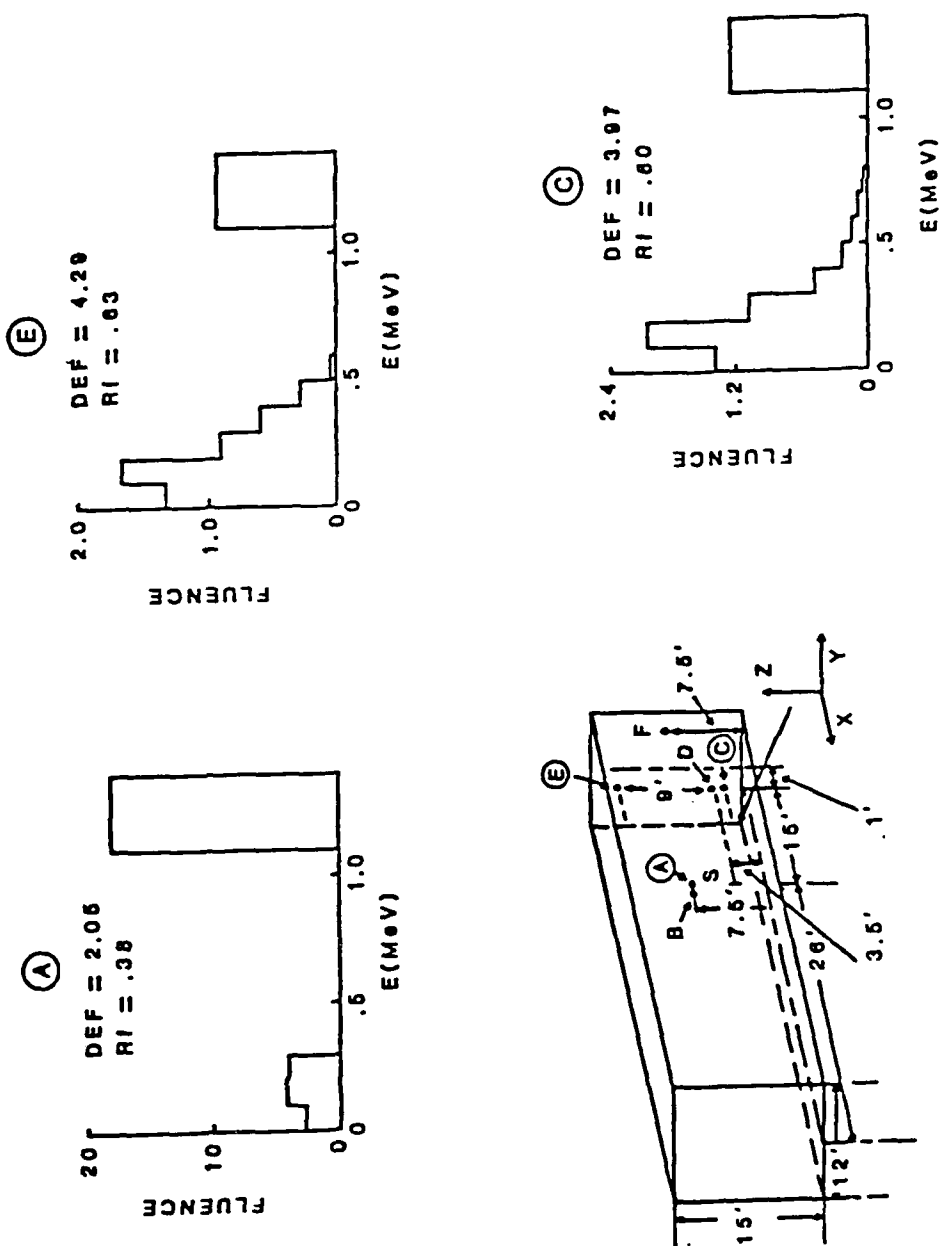
IV.1 MCNP - General Description

The Los Alamos Monte Carlo computer code MCNP^{3,1} is a general purpose Monte Carlo code that can be applied to photon, neutron and coupled neutron-photon transport problems. It has the capability of simulating transport in arbitrary three-dimensional configurations of materials. Cells consisting of the various materials in the problem as well as void cells, are defined by bounding surfaces of first (linear)- and second (curved)-degree. With this code it has been possible for us to perform photon transport calculations in complicated geometries involving several materials. MCNP has its own cross section library, based on the Storm and Israel compilation^{3,2}.

The results of our photon Monte Carlo calculations are expressed in the form of scattered photon spectra characteristic of various Cobalt-60 irradiation sources. The spectrum information obtained was used directly in the estimation of dose enhancement factors in metallized semiconductor materials under irradiation test conditions. It was therefore necessary to simulate as closely as possible the actual physical conditions, both geometrical and material, at the various irradiation test facilities. Four MCNP calculations^{2,5}, and the results obtained, will be discussed. The first three are simulations of actual Cobalt-60 irradiation experiments and fall into the following categories: 1)photon spectra obtained at various positions inside a concrete-walled room in which a Co-60 rod source is placed; 2)photon spectra calculated at various positions inside a standard irradiation test cell, the AECL Gammacell 220; 3)photon spectra calculated for an array of point detectors along the centerline of the NBS water well irradiation chamber. The fourth calculation does not simulate any one experiment in particular, but provides a means for determining the filtration effect of lead shields on scattered Co-60 photon spectra of arbitrary shape. This is accomplished by means of a series of Monte Carlo calculations with monoenergetic photon sources.

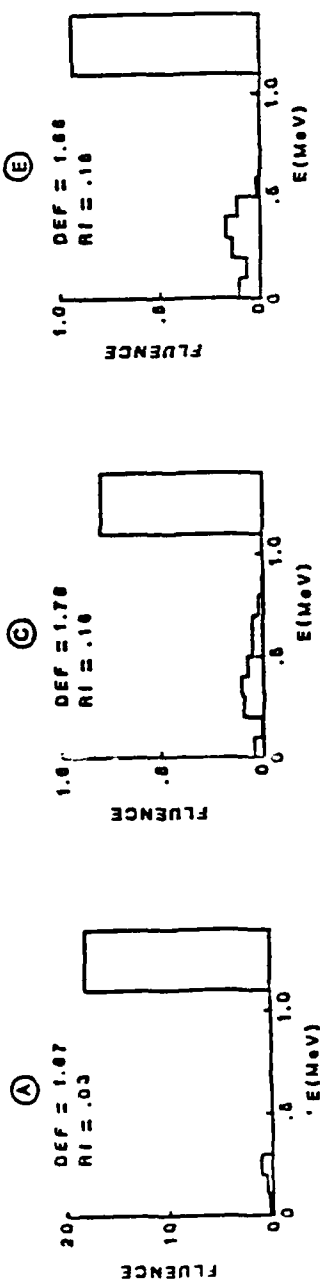
IV.2 Concrete-Walled Room Irradiation Chamber^{2,5}

In the concrete room calculations, fluence spectra were calculated for several source-detector configurations, the major portion of which were done with a Co-60 rod source with an energy spectrum in which downscatter by the rod and cladding are accounted for. In other instances a pure Co-60 photon source with no energy degradation was assumed. The source (see Fig.34) was taken to be a 13" Co-60 rod with center located at a height of 3.5' above the floor a room of dimension 12'x15'x42' (these dimensions are representative of several test facilities). The source position shown in Fig.34 is x=16'(from back wall),

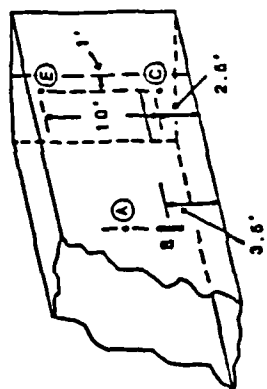


(FLUENCE IN RELATIVE UNITS)

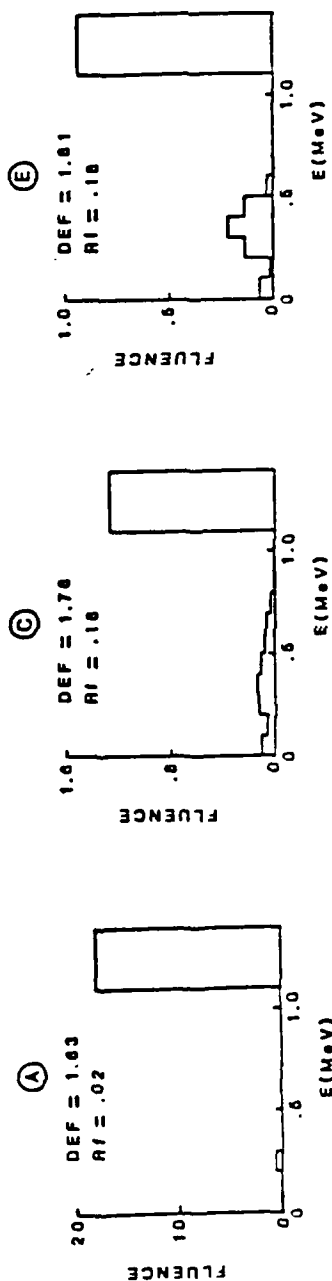
Figure 34. Co-60 source, S, and fluence spectra at 3 detector positions inside concrete-walled room (12 x 15 x 42) (Ref.25).



ONE-HALF OF WALL SURFACE
COVERED BY 1/4" Pb PLATE

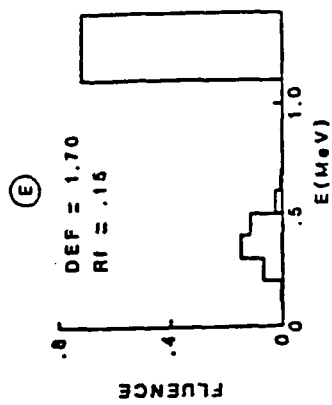


ENTIRE WALL SURFACE
COVERED BY 1/8" Pb PLATE

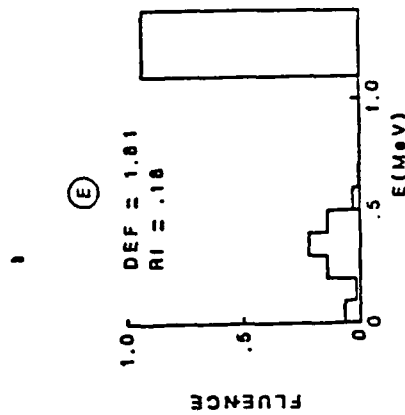


(FLUENCE IN RELATIVE UNITS)

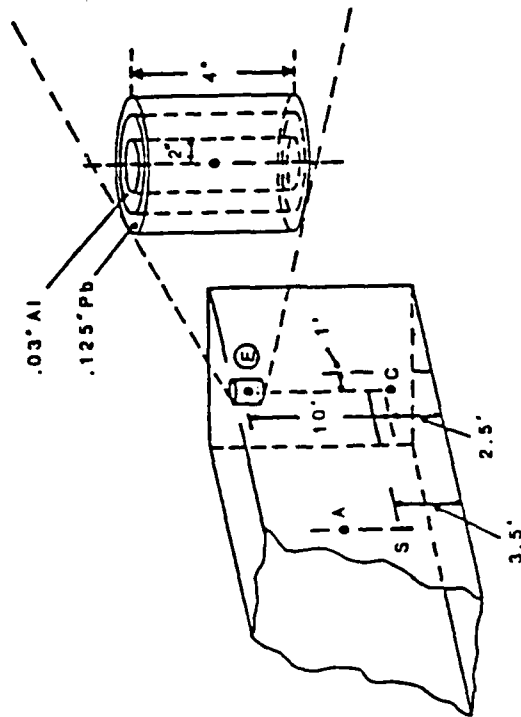
Figure 35. Photon fluence spectra at 3 detector positions in lead-lined (1/4", top row; 1/8", bottom row) concrete-walled room (Ref.25).



I. PHOTON SPECTRUM AT POSITION E
DETECTOR INSIDE CANNISTER SHIELD
(.125"Pb, .03"Al)



II. PHOTON SPECTRUM AT POSITION E
IN COMPLETELY SHIELDED ROOM
(1/8"Pb) WITHOUT CANNISTER.



(FLUENCE IN RELATIVE UNITS)

Figure 36. Photon fluence spectra at detector position E with and without cannister shield (.125"Pb, .03"Al) in concrete room (Ref.25).

y=7.5' (from side wall). Also shown in Fig.34 are scattered Co-60 photon energy spectra, expressed as fluence per source photon per MeV, at detector positions A, C and E. The fluence calculations were made using the "next-event estimator" scheme of MCNP which, as previously stated, calculates in addition to the direct source contribution, the probability of a contribution at a detector point every time a photon undergoes a collision. It is seen that for detectors near the wall (C,E), there is a very large downscattered component (<300 keV). This result is consistent with the energy-angle relation for Compton scatter of photons. For instance, when a 1.25 MeV photon, normally incident on the wall, undergoes a Compton collision, the maximum energy it can have upon re-emerging from the wall after one collision is 362 keV. If multiple scattering occurs, which is highly likely, only a photon of lesser energy can emerge from the wall. Spectral components of higher energy (present in the spectra shown in Fig.34) result from photons emerging at grazing angles from the side walls, floor and ceiling. Angular photon spectra were not obtained in these calculations.

The quantities labelled DEF in the spectra of Fig.34 are the dose enhancement factors for the Au-Si interface of a gold-metallized silicon device (see Ref.25 for the definition of DEF). The other quantity, R_f , is defined as the ratio of the scattered photon fluence to total photon fluence.

In Fig.35 photon spectra are shown for detector points A, C and E with, in one instance, one-half of the wall surface covered by 1/4" lead plate (upper three graphs), and in the other instance, the entire wall surface covered by 1/8" lead plate (lower three graphs). These illustrate the extent to which the Co-60 scattered photon spectrum can be altered by a change in the scatterer material. For these cases, significant filtering of the low energy spectrum components occurs. Finally, in Fig.36 we show the result of a spectrum calculation at detector position E with the detector placed inside a lead-aluminum cannister shield. Clearly, considerable filtering of the low energy component occurs here also.

IV.3 AECL Gammacell 220²⁵

Extensive calculations were performed of the scattered Co-60 photon spectra in the Gammacell 220 irradiation cell. A cutaway view of the Gammacell unit is shown in Fig.37. Photon fluence spectra were calculated for 11 detector positions for two source rod arrangements; 1) 12 source rods placed symmetrically around the irradiation chamber, and; 2) 1 source rod. Of the 11 detectors, 5 were point detectors positioned along the symmetry axis at 1/8", 2", 4", 6", 7-7/8" from the chamber bottom. The remaining 6 were ring detectors, also concentric with the axis of symmetry. The fluence spectra for both the 12 and 1 rod cases

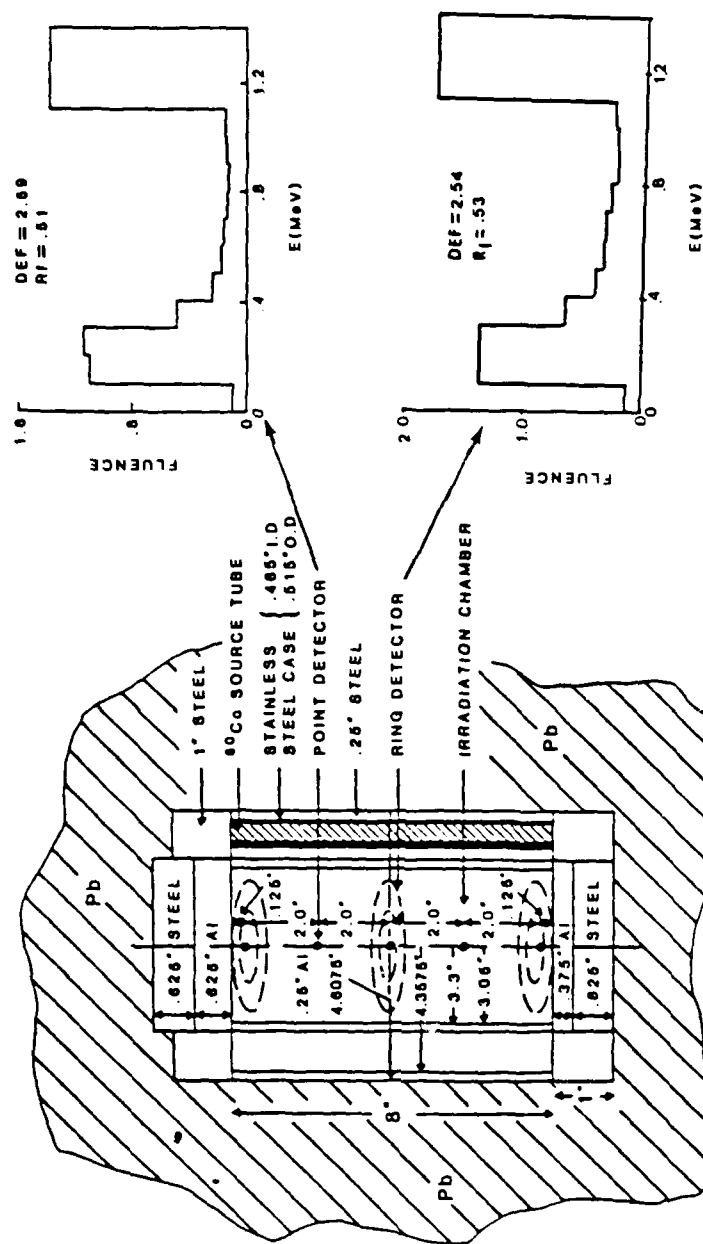


Figure 37. Cutaway view of Gammacell 220 with point(5) and ring(6) detectors shown. Photon fluence spectra at center point and ring (3" radius) detectors for the 12 source rod configuration. Units are $10^{-6} \text{ cm}^{-2}/\text{MeV}/\text{Source Photon (Ref.25)}$.

Table 3.

AECL Gammacell 220

Photon Fluence Spectra at 5 Point Detectors and 6 Ring Detectors (see Fig.37) for Single Source Rod and 12 Source Rod Cases. (Units are 10^{-3} cm $^{-2}$ /MeV/Source Photon). (Ref.25).

Energy Interval (MeV)	Single Source Rod										
	Point Detectors (see Fig.8)					Ring Detectors (see Fig.8)					
	1	2	3	4	5	6	7	8	9	10	11
0 - .1	.1113	.1079	.1086	.1175	.1495	.1566	.1162	.1316	.1431	.1882	.1470
.1 - .2	.1091	.1137	.1148	.1146	.1099	.1168	.1204	.1178	.1352	.1367	.1171
.2 - .3	.9627	.1166	.1191	.1182	.1231	.1089	.1206	.1043	.1090	.1374	.1053
.3 - .4	.4974	.4675	.4666	.4624	.4801	.4761	.5240	.4806	.5341	.6322	.5925
.4 - .5	.2783	.2577	.2453	.2300	.2351	.2802	.2796	.2636	.2740	.4036	.3235
.5 - .6	.2091	.1670	.1929	.1771	.1510	.2288	.2138	.1933	.2473	.3482	.2259
.6 - .7	.1415	.1517	.1530	.1375	.1464	.1531	.1771	.1439	.1776	.2237	.2067
.7 - .8	.1360	.1388	.1477	.1489	.1178	.1248	.1670	.1248	.1388	.2661	.1720
.8 - .9	.1234	.1256	.1444	.1348	.1293	.1180	.1352	.1098	.1352	.1758	.1758
.9 - 1.0	.1078	.1181	.1438	.1201	.1023	.1338	.1617	.1478	.1327	.2669	.1241
1.0 - 1.1	.1165	.1142	.1402	.1204	.1029	.1208	.1486	.1056	.1215	.2013	.1298
1.1 - 1.4	.9389	.1286	.1368	.1260	.9621	.9747	.1458	.9993	.1102	.1770	.1104
DEF	2.89	2.69	2.64	2.72	2.98	2.96	2.62	2.93	2.94	2.56	2.82
R _f	.59	.54	.52	.54	.60	.60	.52	.59	.60	.54	.59
Energy Interval (MeV)	12 Source Rods										
	Point Detectors (see Fig.8)					Ring Detectors (see Fig.8)					
	1	2	3	4	5	6	7	8	9	10	11
0 - .1	.1169	.1049	.0986	.1093	.2473	.1224	.1118	.1502	.1226	.1349	.1321
.1 - .2	.1147	.1153	.1099	.1113	.1174	.1238	.1205	.1237	.1184	.1377	.1192
.2 - .3	.1044	.1121	.1141	.1122	.1385	.1006	.1193	.9642	.1027	.1368	.9887
.3 - .4	.4281	.4777	.4914	.4809	.5339	.4942	.5275	.4685	.5488	.6456	.5298
.4 - .5	.3166	.2573	.2480	.2420	.2514	.3227	.2805	.2716	.3188	.4005	.3085
.5 - .6	.1937	.1679	.1825	.1737	.1646	.2123	.2096	.1802	.2478	.3289	.2177
.6 - .7	.1564	.1580	.1682	.1457	.1354	.1664	.1832	.1573	.1960	.3247	.2023
.7 - .8	.1242	.1323	.1456	.1366	.1274	.1274	.1643	.1344	.1655	.2706	.1795
.8 - .9	.1260	.1279	.1358	.1294	.1199	.1373	.1721	.1097	.1469	.2324	.1006
.9 - 1.0	.1106	.1183	.1508	.1392	.1194	.1138	.1493	.1370	.1437	.2326	.1314
1.0 - 1.1	.1187	.1299	.1594	.1198	.0926	.1188	.1474	.1252	.1309	.2585	.1555
1.1 - 1.4	.9151	.1304	.1387	.282	.9711	.9881	.1486	.1009	.1118	.1779	.1142
DEF	2.94	2.68	2.59	2.67	3.12	2.95	2.60	2.94	2.79	2.54	2.78
R _f	.50	.54	.51	.53	.62	.60	.52	.59	.58	.53	.58

are given in Table 3 of along with the ratios of scattered to total fluence and the Au-Si dose enhancement factors. Typical spectrum plots, photon fluence for the center point detector and for the center 3" radius ring detector, are also shown in Fig. 37 for the 12 rod case.

IV.4 NBS Water Well Irradiator²⁵

Photon energy spectrum calculations were performed for the NBS water well irradiator which consists of a watertight stainless steel cylindrical chamber approximately 12" in height with radius 2", in which the sample to be irradiated is placed. Photon fluence spectra were calculated at 15 point detectors placed 2 cm. apart along the centerline. A drawing of the problem geometry and detector positions is given in Fig.38 along with plots of fluence spectra at three detector points, bottom, center and top. The calculated photon fluence spectra for all 15 detectors are given in Table 4. Figure 39 is a plot of the calculated dose in Si as a function of position on the centerline of the water well irradiation cell. These values were arrived at using the calculated scattered photon spectra at the 15 centerline positions. As can be seen, the predicted dose varies considerably with position. Experimental confirmation has been obtained of the agreement between the position of maximum measured dose and the position of calculated maximum dose³³.

IV.5 MCNP Calculations for the Estimation of Filtration of Low Energy Components of Scattered Photon Spectra by Lead Cylinder Shields

A series of MCNP Monte Carlo calculations was made of scattered photon spectra inside two lead cylinder shields of thickness 1/16" and 1/8". These calculations were done in response to a request from members of the ASTM Subcommittee E10.07 on "Ionizing Radiation Dosimetry and Application for Materials Testing and Processing" at the September, 1985 meeting. The calculations were organized in such a way that the results can be applied to determine the filtration effect of the shield on scattered photon spectra of arbitrary shape. The MCNP computer runs were performed for 12 monoenergetic photon sources, with isotropic angular distributions, uniformly distributed on the surface of the lead shield cannister. Four point detectors were placed at 1/2" intervals from the bottom surface along the cylinder axis (see Fig.40). The source energies chosen were 1.33, 1.17, 1.05, 0.95, 0.85, 0.75, 0.65, 0.55, 0.45, 0.35, 0.25, 0.15 MeV. The filtration effect of the shield on scattered photon spectra of any given shape can be determined by taking the linear combination of monoenergetic photon sources appropriate to the problem. For example, if the scattered photon spectra are known at several detector positions inside, say, a bare-walled concrete room, as shown in Fig.34, the spectrum filtration at these points

by the two lead cannisters can be calculated using the Monte Carlo data tabulation printed in Ref.34. These tables occupy more pages than would be appropriate to present here. However, they also exist on a magnetic medium computer file (floppy disk) and can be easily read into a microcomputer or minicomputer where they can be put to use. This file is available to the microelectronic parts testing community or other qualified researchers who may have an interest in estimating dose enhancement.

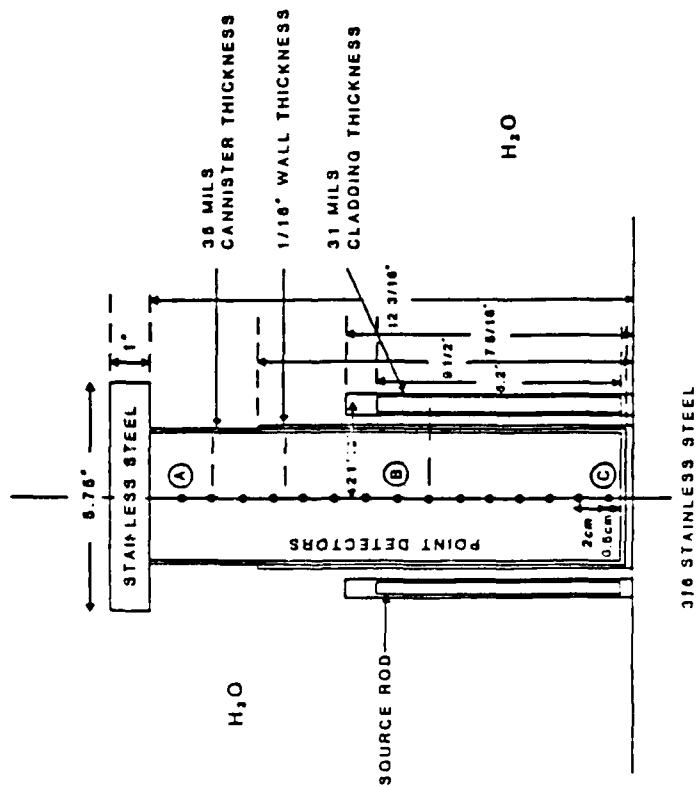
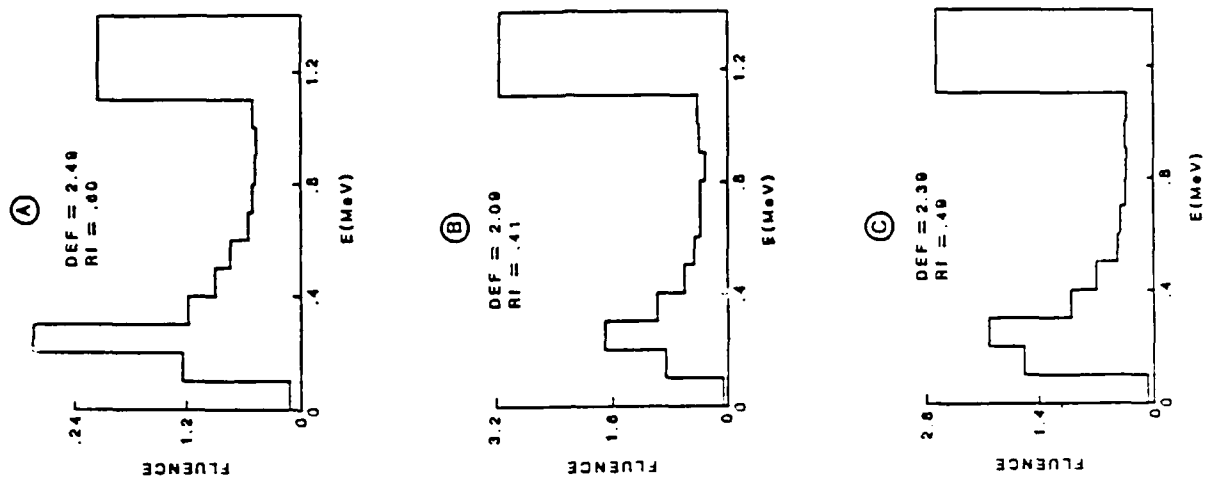


Figure 38. Cutaway view of NBS Water Well Irradiation Cell with 15 centerline point detectors shown; photon fluence spectra at detector positions A,B,C. Units are $10^{-3} \text{ cm}^{-2} \text{ /MeV/Source Photon (Ref.25)}$.

Table 4.

NBS Water Well Irradiation Cell
Photon Fluence Spectra along Centerline (see Fig.38)
(Units are $10^{-3}\text{cm}^{-2}/\text{MeV}/\text{Source Photon}$)

Energy Interval (MeV)	0.5	2.5	4.5	6.5	8.5	10.5	12.5	14.5	16.5	18.5	20.5	22.5	24.5	26.5	28.5
0 - .1	.0713	.0818	.0836	.0842	.0809	.0823	.0779	.0626	.0468	.0350	.0246	.0173	.0143	.0132	.0128
.1 - .2	1.578	1.307	1.346	1.284	1.255	1.148	1.046	.8692	.6762	.4740	.3199	.2307	.1735	.1389	.1239
.2 - .3	2.008	2.518	2.270	2.219	2.185	2.147	1.895	1.701	1.226	.8284	.5629	.3833	.2680	.2228	.2841
.3 - .4	1.104	1.081	1.153	1.207	1.370	1.219	1.157	.9870	.7436	.5251	.3594	.2761	.2128	.1543	.1186
.4 - .5	.7030	.6657	.7068	.7958	.7855	.7536	.6696	.6129	.5008	.3666	.2623	.1823	.1414	.1156	.0892
.5 - .6	.4431	.4668	.5687	.5926	.6460	.6339	.5815	.4717	.3801	.3093	.2210	.1502	.1130	.0924	.0741
.6 - .7	.4111	.4569	.5192	.5524	.5575	.5112	.4928	.3937	.3302	.2546	.1946	.1413	.0969	.0691	.0557
.7 - .8	.3454	.4084	.4257	.4684	.5140	.5592	.4352	.3905	.3102	.2436	.1821	.1353	.0906	.0689	.0512
.8 - .9	.3361	.3867	.4381	.4510	.4436	.4693	.4921	.3271	.2859	.2276	.1553	.1342	.1015	.0702	.0484
.9 - 1.0	.3501	.3603	.4036	.4572	.4089	.4345	.4348	.4147	.2970	.2018	.1808	.1120	.0894	.0623	.0478
1.0- 1.1	.3390	.3837	.4299	.4074	.4145	.4054	.4241	.4327	.2777	.2290	.1639	.1174	.0821	.0687	.0514
1.1- 1.4	2.643	3.409	3.919	4.184	4.280	4.113	3.761	3.157	2.355	1.542	.9931	.6548	.4385	.3026	.2150
DEF	2.39	2.24	2.16	2.12	2.10	2.09	2.09	2.09	2.10	2.11	2.13	2.16	2.20	2.27	2.49
R _f	.489	.442	.415	.404	.403	.404	.406	.413	.418	.444	.468	.489	.513	.542	.597

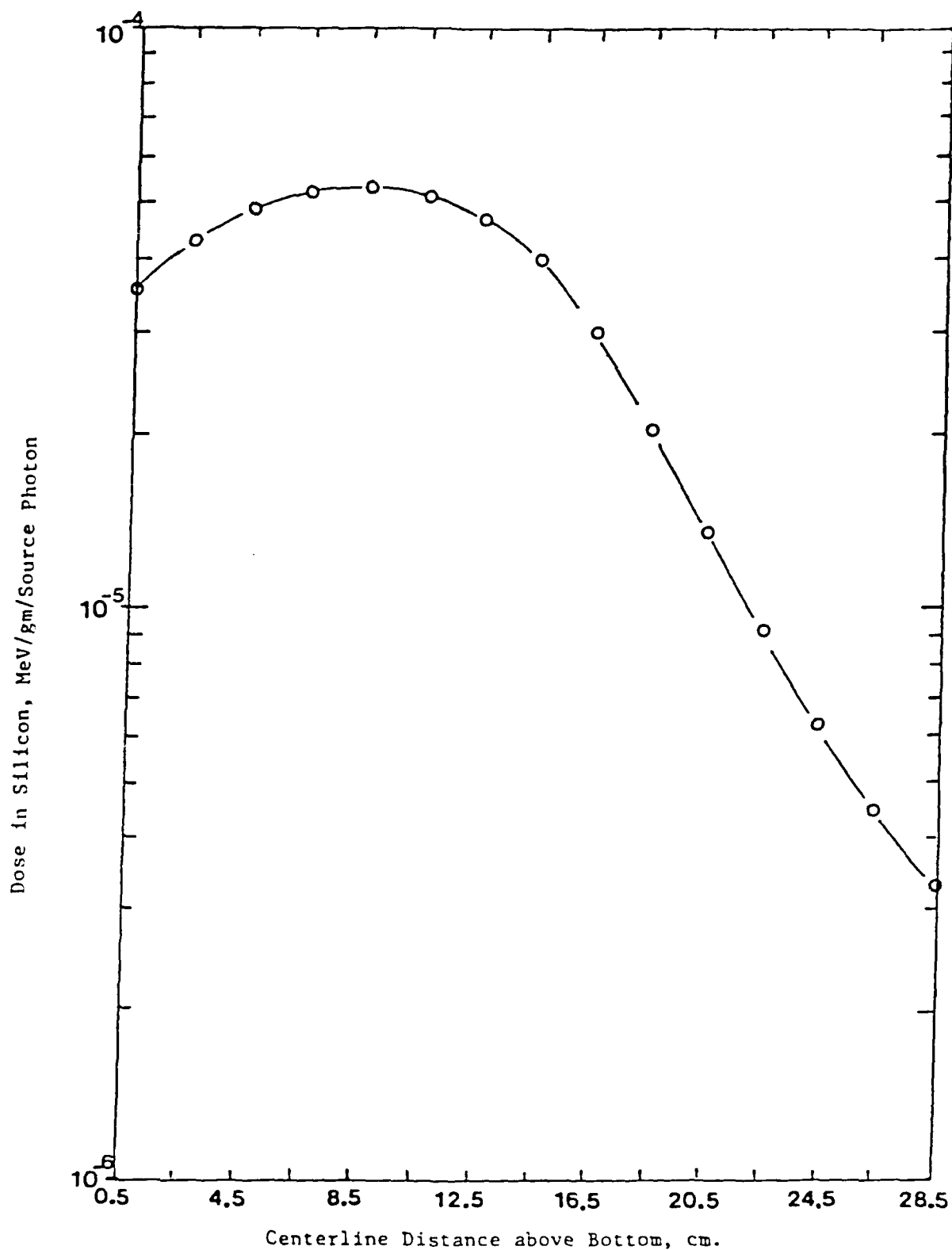


Figure 39. Dose in silicon at 15 point detector positions (see Fig.38) in NBS Water Well Irradiation Cell. Twelve Co-60 source rods (Ref.25).

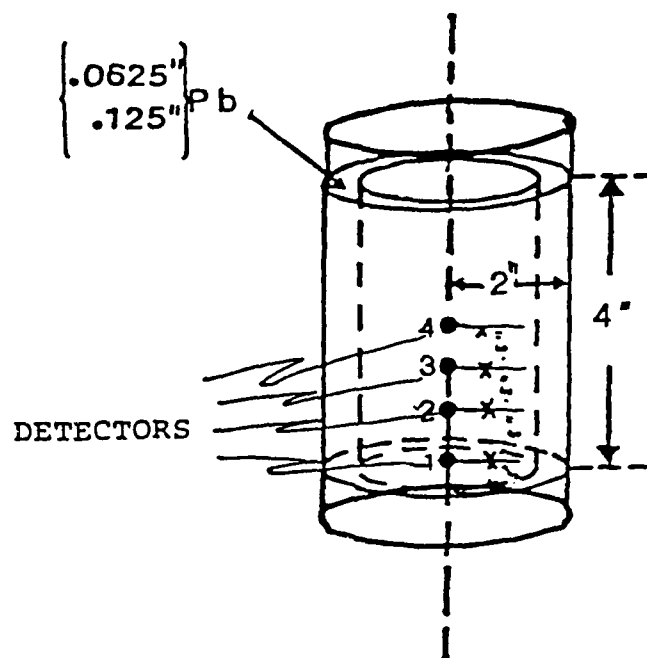


Figure 40. Lead cylinder geometry (Ref.34).

V. REFERENCES

1. T.R. Hill, "ONETRAN: A Discrete Ordinates Finite Element Code for the Solution of the One-Dimensional Multigroup Transport Equation", LA-5990-MS, Los Alamos National Laboratory (1975).
2. J.A. Halbleib and T.A. Mehlhorn, "ITS: The Integrated TIGER Series of Coupled Electron/Photon Monte Carlo Transport Codes", Sandia National Laboratories Report SAND 84-0573 (November 1984).
3. ASTM Subcommittee E10.7, "Standard Practice for Minimizing Dosimetry Errors in Radiation Hardness Testing of Electronic Devices Using Co-60 Sources", American Society for Testing and Materials Standard, to be published in late 1987 or early 1988.
4. W.L. Filippone, S. Woolf and J.C. Garth, "A Comparison of Two Discrete Ordinates Methods for Electron Transport Calculations", Proc. ANS Topl. Mtg. Advances in Reactor Computations, Salt Lake City, Vol.II, 649(1983).
5. W.L. Filippone and S. Woolf, Trans. Am. Nuc. Soc. 46, 435 (1984).
6. S. Woolf, W.L. Filippone, B.D. Ganapol and J.C. Garth, Nuc. Sci. Eng. 92, No.1, 110 (1986).
7. W.L. Filippone, S. Woolf, J.C. Garth and B.D. Ganapol, Trans. Am. Nuc. Soc., 50, 270 (1985).
8. J.C. Garth, E.A. Burke and S. Woolf, "Displacement Damage and Dose Enhancement in Gallium Arsenide and Silicon", to IEEE Trans. Nuc. Sci., NS-32, No. 7, 4382 (1985).
9. L.V. Spencer, "Energy Deposition by Fast Electrons", National Bureau of Standards, NBS Monograph 1 (1959).
10. B.G. Carlson and K.D. Lathrop, in Computing Methods in Reactor Physics, H. Greepspan, C.N. Kelber and DF. Okrent, Eds. (Gordon and Breach, New York, 1968).
11. J.E. Morel, Nucl. Sci. Eng., 71, 64 (1979).
12. M.J. Berger and S.M. Seltzer, "Stopping Powers and Ranges of Electrons and Positrons", U.S. Dept. of Commerce, National Bureau of Standards Report No. NBSIR 82-2550, (August, 1982).

13. B.D. Ganapol, Nucl. Sci. Eng., 92, No.2, 272 (1986).
14. S. Woolf and A.R. Frederickson, IEEE Trans. Nuc. Sci., NS-30, No.6, 4371 (1983).
15. J.C. Garth, W.L. Chadsey and R.L. Sheppard, J., IEEE Trans. Nuc. Sci., NS-22, No.6, (1975).
16. J.C. Garth, E.A. Burke and S. Woolf, IEEE Trans. Nuc. Sci., NS-27, No.6, (1459 (1980)).
17. E.A. Burke, N.J. Grossbard and L.F. Lowe, "Calculated Cross Sections for Atomic Displacements Produced by Electrons in the 1.0-3.0 MeV Energy Range", AFCRL-65-286, Air Force Cambridge Research Laboratories, April 1965 (NTIS accession number AD 616245).
18. J.C. Garth and S. Woolf, Trans. Am. Nuc. Soc., 52, 390 (1986).
19. J. C. Garth, IEEE Trans. Nucl. Sci., NS-25, No.6., 1598 (1978).
20. A.A. Shkurpelov, A.P. Elokhin and V.P. Veselov, Sov. At. Energy, 52, 440(1982).
21. S. Woolf and J.C. Garth, IEEE Trans. Nucl. Sci., NS-33, No.6, 1252 (1986).
22. J.A. Wall and E.A. Burke, "Dose Distributions at and near the Interface of Different Materials Exposed to Cobalt-60 Radiation", AFCRL-TR-0074 (December, 1974).
23. W.L. Chadsey, "POEM: A Fast Monte Carlo Code for the Calculation of X-Ray Photoemission and Transition Zone Dose and Current", AFCRL-TR-75-0324 (1975).
24. K. Kerris and S.G. Gorbics, HDL-TR-2082, "Experimental Determination of the Low-Energy Spectral Component of Cobalt-60 Sources", (April 1986).
25. S. Woolf and E.A. Burke, IEEE Trans. Nucl. Sci., NS-31, No.6, 1089 (1984).
26. R.D. Evans, The Atomic Nucleus, P. 693, McGraw-Hill, New York (1955).
27. L.V. Spencer, Phys. Rev., 98, 1597 (1955).
28. J.N. Bradford, IEEE Trans. Nucl. Sci., NS-33, No.6, 1271 (1986).

29. R.N. Hamm and R.H. Ritchie, Oak Ridge National Laboratory Health and Safety Research Division, Private Communication, (July, 1985).
30. M.J. Berger, Methods in Computational Physics, Vol. 1, Academic Press, New York (1963).
31. Los Alamos Radiation Transport Group(X-6), "MCNP - A General Monte Carlo Code for Neutron and Photon Transport", LA-7396-M, (Revised April 1981), Version 3, RSIC Computer Code Collection CCC-200 (1983).
32. E. Storm and H.I. Israel, "Photon Cross Sections from 0.001 to 100 MeV for Elements 1 through 100", LASL Report LA-2753 (1967).
33. J.C. Humphreys, National Bureau of Standards, Private Communication, March 1984.
34. J.C. Humphreys, "Minutes of the ASTM E10.07 Task Groups (2) and (3) at NBS on Sept. 10 and 11, 1985", Oct. 28, 1985.